Faculty of Engineering of University of Porto

FEUP

Smart Nanoparticles: an Approach to Fight Brain Cancer

Érica Alexandra Araújo Serra

Master Dissertation
Master's in Biomedical Engineering

Supervisor: Prof. Dr. Maria do Carmo Pereira
Co-Supervisor: Dr. Maria João Ramalho

June 2023

Financial Support

This work was financially supported by: LA/P/0045/2020 (ALiCE), UIDB/00511/2020 and UIDP/00511/2020 (LEPABE), funded by national funds through FCT/MCTES (PIDDAC); project EXPL/NAN-MAT/0209/, funded by FEDER funds through COMPETE2020 – Programa Operacional Competitividade e Internacionalização (POCI) and by national funds (PIDDAC) through FCT/MCTES; Project 2SMART - engineered Smart materials for Smart citizens, with reference NORTE-01-0145-FEDER-000054, supported by Norte Portugal Regional Operational Program (NORTE 2020), under the PORTUGAL 2020 Partnership Agreement, through the European Regional Development Fund (ERDF). FCT supported M.J.R. under the Scientific Employment Stimulus - Individual Call – (CEEC-IND/01741/2021). This project has received funding from the European Union's Horizon 2020 research and innovation programme under grant agreement No 958174; and from national funds through FCT (M-ERA-NET3/0001/2021).

Acknowledgments

I would like to express my sincere gratitude to all those who have supported me throughout my dissertation journey.

I would like to start by expressing my gratitude to my supervisors, Prof. Dr. Maria do Carmo Pereira and Dr. Maria João Ramalho, for their exceptional scientific guidance and invaluable knowledge transmitted along my research path. I extend my gratitude to my esteemed laboratory colleagues at LEPABE for their valuable collaboration. In addition, I would like to express my appreciation to Dr. Paula Soares and Dr. Jorge Lima from the Cancer Signaling and Metabolism Group of the Institute for Research and Innovation in Health Sciences (i3S) for providing the necessary facilities for the cellular studies.

I extend my heartfelt appreciation to all my friends who have been by my side and provided me support throughout this year.

Finally, but certainly most importantly, I express my deepest gratitude to my family for their unwavering support, unconditional love and total trust in me. They have consistently been my safe place and the most attentive listeners and confidants I could ever ask for.

Resumo

O Glioblastoma Multiforme (GBM) é um Glioma de grau IV e é um tumor cerebral altamente mortal. Este tumor, extremamente invasivo, não responde satisfatoriamente ao tratamento convencional, levando apenas a um ligeiro aumento da esperança de vida dos pacientes. A Gemcitabina (GEM) tem sido estudada para o tratamento do GBM e por não ser um agente alquilante, permite ultrapassar a resistência mediada pela proteína MGMT, uma das principais limitações da terapia convencional. A administração intranasal de medicamentos permite alcançar o cérebro mais eficazmente, superando a barreira hematoencefálica. A utilização de nanopartículas (NPs) para a entrega de fármacos por via intranasal apresenta vantagens consideráveis, uma vez que permite melhores condições de fornecimento de fármacos através de polímeros mucoadesivos, tais como o quitosano (CH).

Este trabalho visou a produção de NPs de ácido poli(láctico-co-glicólico) (PLGA) funcionalizadas com CH para a entrega intranasal de GEM para o tratamento do GBM. Para uma otimização mais precisa e eficaz do protocolo de preparação das NPs, foi utilizado o desenho experimental. Para o efeito, foi implementado um design composto central, de forma a produzir NPs otimizadas com as características adequadas para a administração intranasal (tamanho inferior a 200 nm, baixa polidispersão (PDI) e potenciais zeta positivos). As NPs produzidas apresentaram características físico-químicas adequadas e dentro do previsto pelo desenho experimental. O perfil de libertação da GEM foi estudado, revelando uma libertação lenta e controlada que é acelerada quando usada uma enzima responsável pela degradação da camada de CH externa, a lisozima.

O efeito antiproliferativo das NPs preparadas foi estudado em duas linhas celulares humanas de GBM (U251 e T98G), com diferentes expressões da proteína MGMT. Os ensaios celulares permitiram provar que as NPs de CH-PLGA com GEM encapsulada são capazes de provocar a inibição da sobrevivência celular. Além disso, foi demonstrada a biocompatibilidade das NPs de CH-PLGA.

Palavras-chave: Glioblastoma Multiforme; Gemcitabina; Nanopartículas; Ácido poli(láctico-co-glicólico); Quitosano; Entrega Intranasal; Desenho experimental.

Abstract

Glioblastoma Multiforme (GBM) is a grade IV Glioma and is a highly deadly brain tumor. This extremely invasive tumor does not respond satisfactorily to conventional treatment, leading only to a slight increase in the life expectancy of patients. Gemcitabine (GEM) has been studied for the treatment of GBM and because it is not an alkylating agent, it allows overcoming MGMT protein-mediated resistance, a major limitation of conventional therapy. Intranasal drug delivery allows reaching the brain more effectively by overcoming the blood-brain barrier. The use of nanoparticles (NPs) for intranasal drug delivery has considerable advantages, as it allows better drug delivery conditions through mucoadhesive polymers, such as chitosan (CH).

This work aimed to produce poly(lactic-co-glycolic acid) (PLGA) NPs functionalized with CH for intranasal delivery of GEM for the treatment of GBM. For a more precise and effective optimization of the NPs' preparation protocol, experimental design was used. For this purpose, a central composite design was implemented to produce optimized NPs with the appropriate characteristics for intranasal administration - size less than 200 nm, low polydispersion index (PDI) values and positive zeta potentials. The produced NPs presented adequate physicochemical characteristics and within the predicted by the experimental design. The release profile of GEM was studied, and the results revealed that the NPs were able to maintain a slow and sustained release. Additionally, the results showed that in the presence of lysozyme - enzyme responsible for the degradation of the outer CH layer – the released was faster.

The antiproliferative effect of the prepared NPs was studied in two human GBM cell lines (U251 and T98G), with different expression of the MGMT protein. Cellular assays allowed to prove that GEM loaded CH-PLGA NPs are able to cause inhibition of cell survival. In addition, the biocompatibility of CH-PLGA NPs was demonstrated.

Keywords: Glioblastoma Multiforme; Gemcitabine; Nanoparticles; Poly(lactic acid-co-glycolic acid); Chitosan; Intranasal Delivery; Experimental Design.

Contents

List of Figures

List of Tables

Abbreviations and Symbols

Lists of abbreviations

BBB	Blood-Brain Barrier
CCD	Central Composite Design
CED	Convection-enhanced delivery
CH	Chitosan
CNDs	Carbon Nitride Dots
CNS	Central Nervous System
CSF	Cerebrospinal Fluid
CT	Chemotherapy
CTX	Chlorotoxin
DAC	Decitabine
DCM	Dichloromethane
DDSs	Drug Delivery Systems
DLS	Dynamic Light Scattering
DMEM	Dulbecco's Modified Eagle Medium
DMSO	Dimethyl Sulfoxide
DNA	Deoxyribonucleic Acid
DoE	Design of Experiments
EA	Ethyl Acetate
EE	Encapsulation Efficiency
FBS	Fetal Bovine Serum
FDA	Food and Drug Administration
FTIR	Fourier-Transformed Infrared Spectroscopy
GBM	Glioblastoma Multiforme
GEM	Gemcitabine
GSCs	Glioma Stem Cells
HA	Hyaluronic Acid
LNC	Lipid Nanocapsule

MGMT	O^6-Methylguanine-DNA Methyltransferase
MTIC	5-(3-methyltriazen-1-yl) imidazole-4-carboxamide
NPs	Nanoparticles
NVU	Neurovascular Unit
PBCA	Polybutylcyanoacrylate
PEG	Polyethylene Glycol
PDI	Polydispersity Index
PLGA	Poly (lactic-co-glycolic acid)
PVA	Polyvinyl Alcohol
RT	Radiation Therapy
SD	Standard Deviation
SRB	Sulforhodamine B
TEM	Transmission Electron Microscopy
TCA	Trichloroacetic acid
Tf	Transferrin
TMZ	Temozolomide
VPA	Valproic Acid
WHO	World Health Organization

Lists of symbols

μ_e	Electrophoretic mobility
ε_r	Dielectric constant
ε_0	Permittivity in vacuum
f(Ka)	Henry's Function
η	Viscosity
ζ	Zeta Potential
v	Velocity
E	Electric field
k	Boltzmann constant
T	Absolute temperature
D	Translation diffusion coefficient
R_H	Hydrodynamic radius
A	Absorbance
ε	Molar Absorption Coefficient
c	Concentration
d	Path length of the beam
I_0	Intensity of the incident light beam
I	Intensity of the light that reach the detector

Chapter 1

Introduction

Glioblastoma Multiforme (GBM) is the most invasive and deadly brain tumor in adults [1]. Despite the treatments available, this cancer is still incurable and has an average life expectancy of 14 months [2].

Gemcitabine (GEM) is a nucleoside analog and is currently approved and used in the treatment of solid tumors [3]. This therapeutic drug is an effective cancer cell killer, and its potential has been studied for the treatment of GBM. GEM is not an alkylating agent, and thus it can overcome MGMT-mediated resistance, one of the main limitations of conventional treatment with the gold-standard drug (temozolomide (TMZ)) [4].

Drug delivery to the brain presents several challenges since the blood-brain barrier (BBB) has a permeable selectivity and restricts therapeutic efficacy. Thus, new methods of drug delivery to the brain have been studied [5]. Nose-to-brain delivery is a successful and non-invasive method for delivering medications into the brain, which allows overcoming the BBB [6]. The use of nanoparticles (NPs) for intranasal drug delivery has been implemented and numerous mucoadhesive polymers are used to prolong the period of adherence in the nasal cavity, such as chitosan (CH) [7].

CH and PLGA are among the most popular nanomaterials for brain delivery due to being FDA-approved, highly biocompatible, and biodegradable [8].The present work proposes the production of poly(lactic-co-glycolic acid) (PLGA) NPs functionalized with CH for the intranasal delivery of GEM for GBM therapy. This nanosystem is designed for nose-to-brain delivery, which enables a more facilitated delivery of the drug by circumventing the BBB.

1.1 - Objectives

This work has as main objectives the production of GEM-loaded CH-PLGA NPs for GBM therapy and their optimization by implementing experimental design. Another purpose of this study is to analyze the controlled release of the drug over time under physiological conditions. Finally, the performance of *in vitro* assays, to study the antiproliferative effect of the prepared NPs. For this, two human cell lines, T98G and U251, were used.

1.2 – Structure of the Dissertation

This dissertation is organized according to the following topics in the order in which they are mentioned. Chapter 1 gives an introduction, addressing the most important topics in the course of the work. Chapter 2, in which the state-of-the-art of the subject is presented, addresses in the limitations of GBM treatment and presents an overview of the recent progresses for GEM delivery. Chapter 3, materials and methods, presents the methodologies used in this project. Chapter 4 consists of the results and their discussion. Lastly, Chapter 5 presents this work's main conclusions and discusses the plans for future work.

1.3 - Dissertation Output

The research work was carried out at LEPABE – Laboratory for Process Engineering Environment, Biotechnology and Energy at the Faculty of Engineering of the University of Porto. The *in vitro* studies were performed at i3S – Institute for Research and Innovation in Health.

This work was presented in a conference:

- Serra, Érica., Loureiro, Joana. A., Ramalho, Maria João and Pereira, Maria Carmo. Mucoadhesive nanoparticles for the nose-to-brain delivery of gemcitabine for glioblastoma therapy in 16th Encontro de Investigação Jovem da Universidade do Porto (IJUP), 10-12 May 2023, Porto, Portugal (*oral presentation*).

Chapter 2

State of the Art

2.1 - Glioblastoma Multiforme

Gliomas accounts for almost 80% of all malignant brain tumors [1]. These tumors arise from glial cells and are classified by the World Health Organization (WHO) from grades I to IV, according to different factors such as their histological features and survival rates [9]. GBM is a grade IV Glioma, and it is the most aggressive and most common brain tumor in adults, accounting for 77% of all malignant brain tumors [10] and more than half of all gliomas [11]. The average age of people diagnosed with GBM is 64 years and the prevalence of this cancer in children is lower [11]. GBM displays no discernible morphological distinctions between adults and children. However, variations in the proliferative activity of tumor cells have been observed, with children exhibiting a higher proliferation index. Several studies carried out in different countries have shown a higher occurrence of this tumor in males compared to females [12].

GBM is a primary brain neoplasm comprising a phenotypically heterogeneous tumor set. These tumors can be categorized into two groups based on their origin: primary GBM and secondary GBM. Primary GBM consists of 90% of the cases and occurs when the tumor develops *de novo*, from normal glial cells that have undergone tumorigenesis [12]. This type of tumor stands out for its rapid proliferation, growing in about 3 months [9], and typically occurs in patients above 55 years old [13]. The remaining GBM cases are classified as secondary and develop from the progression or transformation of lower-grade gliomas. These have a better prognosis than primary GBM and occur in younger patients, with a mean age of 44 years [14]. Although the genetic properties and the tumorigenesis of primary and secondary GBMs are distinct, there are no differences in their histological grounds [15].

GBM tumors exhibit a large genetic heterogeneity and rapid proliferation rates that are associated with patients' short life-expectancy. However, the ability of this tumor to spread to other organs is low, considering the small number of individuals with GBM extracranial metastases that have been recorded. This arises from the restricted life expectancy of patients, which is inadequate for substantial growth of metastatic tissues [16]. Furthermore, the absence of a lymphatic system in the brain hinders the lymphatic dissemination of tumor cells [17].

The etiology of GBM is poorly understood since most tumors occur sporadically and spontaneously [18]. Familial occurrence of gliomas has been reported, with a genetic predisposition to hereditary gliomas observed in 5-10% of cases [12]. To identify risk factors, different studies have been carried out and to date, the only evidence has been found regarding ionizing radiation [19]. A higher incidence of GBM is also associated with certain rare genetic diseases such as tuberous sclerosis, neurofibromatosis type I and type II, retinoblastoma, and Turcot syndrome [20].

2.1.1 - Conventional Diagnosis and Treatment

GBM symptoms depend on the location of the tumor and the pressure it is putting on, but the most common symptoms are persistent headaches, double or blurred vision, loss of appetite, gradual speech difficulty, ataxia, frequent syncope, and the occurrence of seizures in people who are not diagnosed with epilepsy. As these symptoms are very unspecific, GBM is often misdiagnosed at an early stage [9]. The diagnosis of GBM is achieved by tomographic imaging techniques, such as magnetic resonance imaging (MRI). This technique allows to define the size, shape, and location of the tumors [2]. Nonetheless, the definitive diagnosis involves histopathological examination after surgical resection [9].

Conventional treatment of GBM begins with the maximum possible surgical removal of the tumor, followed by radiation therapy (RT) and chemotherapy (CT) [2]. The treatment depends on several factors, and it is necessary to have an individualized perspective of each patient, considering the patient's age, time of diagnosis, and if it is the first case or a recurrence of the tumor [1].

Since GBM cannot be completely removed because it infiltrates the surrounding tissues, RT and CT are required after surgery. The standard treatment, known as the Stupp protocol, consists of localized RT, 5 times a week over 6 weeks, combined with adjuvant CT with TMZ [2]. Despite the mentioned treatments, GBM is still incurable [13]. The Stupp protocol does not bring satisfactory results and leads to a mean survival rate of 14-15 months, and the probability of reaching 2 years of survival is about 26.5% [2].

The use of TMZ has several limitations such as its high toxicity and low bioavailability in the target tissues [21]. This low bioavailability is because TMZ converts to its active metabolite (3-methyl-(triazen-1-yl)imidazole-4-carboxamide, MTIC) after its administration, and the low permeability of MTIC across the BBB is reflected in a low pharmacological activity [22]. TMZ is

an alkylating agent and its function is based on the methylation of DNA purine bases in O^6-guanine, N^7-guanine, and N^3-adenine, thus inducing cell apoptosis [23].

TMZ effectiveness in the treatment also depends on factors intrinsic to the genetic background of the GBM. Several molecular biomarkers provide important information for diagnosing and monitoring GBM, examples of which are the MGMT (O^6-methylguanine-DNA methyltransferase) promoter methylation [13]. The MGMT gene encodes a DNA damage repair protein that plays a crucial role in the repair of alkyl adducts at the O^6 position of guanines, restoring those bases to DNA [24]. By removing methyl adducts from the O^6 position of guanine, MGMT antagonistically affects TMZ's activity [23]. Patients with GBM may have the MGMT gene methylated or not, and this variation influences resistance to therapy. As a result of the methylation of the MGMT promoter, the expression of MGMT is reduced, resulting in increased chemosensitivity to alkylating agents like TMZ [23][24]. According to several studies, in patients treated with alkylating agents, MGMT methylation has been associated with better overall survival and represents a good prognostic marker in GBM [24]. However, the percentage of unmethylated MGMT promoter in GBM cases is approximately 65%, which means this treatment strategy is limited to a minority of patients [25].

In sum, not only is the current treatment ineffective for patients with unmethylated MGMT promoter, but it is also toxic for those who may benefit from the effectiveness of alkylating agents. The use of TMZ presents a high risk of causing DNA damage to healthy cells, creating the need for additional therapeutic approaches [2]. In this way, non-alkylating agents have been explored as an alternative treatment for patients with an unmethylated MGMT [26].

2.2 - Drug repurposing in GBM

To increase the survival rate and quality of life of patients with GBM, the need for alternative therapies has emerged. In this sense, researchers have explored different drugs and different strategies for their administration. Most recently, drug repurposing has been explored as potential approach for GBM [4]. The concept of drug repurposing refers to the use of previously approved medications for new purposes, other than their traditional ones. This repurposing reduces research costs and the development time of a drug since these drugs have already undergone a rigorous research process [27]. Last years, several drugs have been studied for repurposing in GBM and some have shown potential activity to treat this cancer [28].

In particular, the potential use of FDA-approved non-alkylating chemotherapeutic agents to treat GBM has been envisaged as a promising approach to overcome the resistance to treatment associated with the use of alkylating agents [29]. Some examples of non-alkylating drugs being evaluated for GBM therapy are metformin, valproic acid (VPA), memantine, mefloquine [27] and GEM [4].

Metformin is currently used in the treatment of type 2 diabetes mellitus and its effect on inhibiting tumor cell growth in GBM has been studied in several clinical trials [30]. A study by Seliger et al. (2020) showed that the use of metformin alone or combined with other drugs, in

patients newly diagnosed with GBM, did not increase tumor progression [31]. The efficacy of this antidiabetic drug as a neo-adjuvant compound together with TMZ and RT was evaluated in a recent clinical trial conducted in 33 subjects with GBM [32]. The results proved to be favorable, especially for patients with unmethylated MGMT, since there were no adverse effects from metformin administration.

VPA is a drug used in the treatment of epilepsy and has emerged as a potential agent against GBM. Four clinical trials conducted in newly diagnosed GBM patients did not demonstrate an improvement in patient survival or tumor progression when administered VPA [33]. The authors further concluded that VPA administration helped in controlling patients' seizures. The study by Krauze et al. (2015) evaluated the addition of VPA to conventional treatment with RT and TMZ, in 37 patients [34]. The addition of this drug was well tolerated, and the authors suggest further investigation in a phase III study.

Memantine (a drug used for Alzheimer's disease) and mefloquine (an antimalarial drug) were studied to determine the maximum tolerated dose of both in combination with TMZ [35]. In this phase I clinical trial it was concluded that these drugs can be safely combined with TMZ in patients recently diagnosed with GBM.

2.2.1 - Gemcitabine for the treatment of GBM

GEM is a nucleoside analog and is currently approved and used in the treatment of solid tumors such as breast and ovarian cancer, non-small cell lung cancer, bladder and pancreatic cancer [3]. This chemotherapeutic agent is an effective cancer cell killer, causing cells to die by blocking DNA polymerase activity and inhibiting further DNA synthesis in the cells. When GEM enters the cells, it is metabolized into gemcitabine triphosphate and gemcitabine diphosphate before attacking DNA [36]. Additionally, as GEM is not an alkylating agent it can overcome MGMT-mediated resistance and therefore serve as an alternative treatment for GBM, especially for patients with an unmethylated MGMT promoter [4]. The chemical structure of GEM is shown in Figure 1.

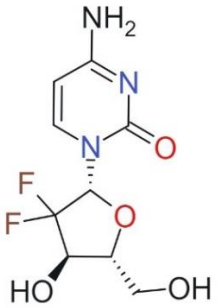

Figure 1 - Chemical Structure of GEM (drawn in MarvinSketch).

Preclinical research has shown that GEM has strong anti-glioma properties *in vitro* and *in vivo* [38]. Carpinelli et al. (2022) investigated the *in vitro* effects of GEM on glioma rat cells

(C6) as well the *in vivo* influence of this drug on C6 brain tumors implanted in Wistar rats [39]. The *in vitro* results showed an alteration in cell cycle progression and an increase in cell apoptosis. *In vivo*, a reduction in tumor volume and a significant delay in tumor growth were observed. Additionally, this drug can also be used in combination with other chemotherapeutic drugs or with RT. In fact, GEM has proved to be an excellent radiosensitizer when compared to conventional TMZ therapy and has already been evaluated in this regard in patients with GBM [40].

However, the use of GEM in combination with RT for GBM has shown contradictory results in clinical trials. In a phase II clinical trial with 30 patients conducted by El-Naggar et al. (2016), the combination of GEM with RT in newly diagnosed GBM was evaluated [40]. The authors concluded that a regimen consisting of GEM and RT is well tolerated. Additionally, GEM and its metabolites showed long retention time in the tumor tissue, allowing for the accumulation of sufficiently high drug concentrations in the tumor for radiosensitization, which prevented systemic effects of RT. On the other hand, Zanten et al. (2017) conducted a phase II clinical trial with 9 pediatric patients newly diagnosed with high-grade glioma to evaluate the combined effect of GEM with RT [41]. The authors verified that although well tolerated, no improvement was observed in therapeutic outcomes.

These contradictory results may be due to its short plasma half-life, poor BBB penetration, and dose-limiting toxicity [38]. In this way, to improve the efficacy of GEM in the treatment of GBM, factors such as penetration into the BBB, concentration of the drug at the target site and a reduction in the toxicity need to be improved. To overcome these challenges, several strategies have been studied regarding the method of delivery of this drug, highlighting the encapsulation of GEM in nanomedicines [4].

2.3 - Nanomedicine

Nanotechnology is dedicated to the study and control of matter with dimensions between 1 and 1000 nm, as well as the development of applications of materials at this scale [42]. In the space of approximately half a century, the science that studies materials at the nanoscale have become the basis of various industrial applications. More specifically, in the pharmaceutical and medicine fields, medical devices including drug delivery systems (DDS) and diagnostic biosensors have been significantly impacted by nanotechnology [43].

To overcome the limitations and improve drug properties *in vivo*, nanomedicine has emerged as a promising strategy [44]. The use of NPs, due to their nanometric size presents important improvements in the treatment and detection of cancer [45].

During the last decades, the interest in research around drug delivery using DDS based on NPs has undergone a considerable increase [45]. The use of these systems presents significant advantages, as it allows restricting the delivery of the drug to a specific site as well as controlling the rate of drug release. NPs can provide a therapeutic action to areas of the body

that otherwise could not be reached, enabling an increase in the therapeutic benefits and also minimizing the side effects [44].

NPs size is between 10 nm and 1000 nm, however for applications in the medical field, the preferred size is less than 200 nm. The shape and size of NPs affect their biodistribution, toxicity and ability to accumulate at specific sites in the human body. In addition to size influencing the performance of NPs as DDS, manipulation of their surface characteristics also allows generating the optimal system. Modifying the surface of NPs with molecules that have specific properties and affinity for the cellular receptors that they are intended to target allows drugs to be transported to tissues in the human body that may have been previously inaccessible and optimizes their delivery [46].

Different types of NPs can be applied in DDS for cancer treatment. These are divided into three types classified as organic NPs, inorganic NPs, and hybrid NPs [47]. Regarding the organic NPs, these are divided into different materials, such as lipids and polymers. The lipid-based NPs include liposomes, which have been widely studied for this purpose and their application is common in different types of cancer. The polymeric-based NPs, synthesized from natural or synthetic materials, include polymeric NPs, polymeric micelles, and dendrimers. These NPs exhibit relevant capabilities in the loading and delivery of therapeutic agents [48]. One of the most used polymers in drug delivery systems is PLGA since it shows good biocompatibility and biodegradability [47].

Inorganic NPs such as gold NPs, carbon nanotubes, silica NPs, quantum dots, and magnetic NPs have also been studied [47]. The main types of NPs used in DDS are illustrated in Figure 2, respectively polymeric and lipid NPs, belonging to the group of organic NPs and some examples of inorganic NPs.

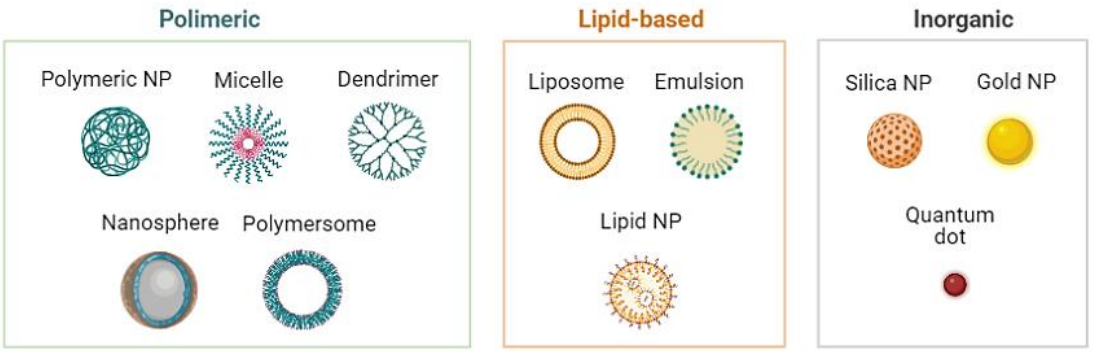

Figure 2 - Different types of NPs used in drug-delivery systems.

Hybrid NPs consist of the combination of different materials in their constitution, which can be both organic or inorganic, or a combination of both. Examples of these NPs are, respectively, lipid-polymer hybrid NPs or liposome-silica hybrid NPs [47].

2.3.1 - Drug Delivery Strategies to the brain

The brain has five barrier interfaces that protect the central nervous system (CNS), and the BBB is the most selective physical barrier. The BBB acts as a highly selective semipermeable barrier that keeps blood-borne solutes from non-selectively entering the extracellular fluid of the CNS [49].

BBB function results from a combination of brain cells known as the neurovascular unit (NVU), which includes brain endothelial cells, neurons, mural cells, microglia, and astrocytes. A complex network of tight junctions seals the paracellular space within the endothelial cells, creating an uninterrupted barrier that preserves cognitive function. The astrocytes, pericytes, and basement membrane surrounding the endothelial cells help to create this protective shield [50]. The structure of the BBB is illustrated in Figure 3.

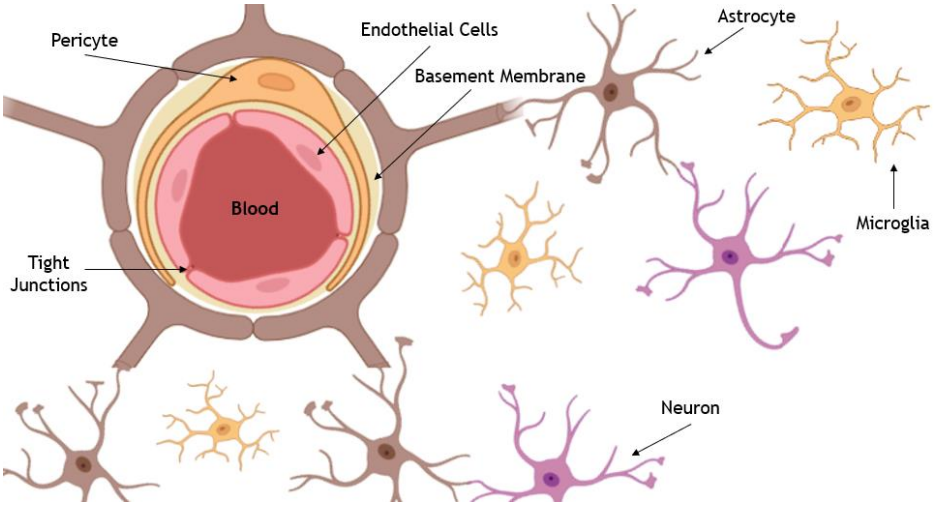

Figure 3 - Schematic illustration of the BBB.

Only a few molecules can pass across the BBB without the aid of transporters. Gases like oxygen and carbon dioxide as well as small and lipid-soluble compounds with a molecular weight under 400 Da or possessing fewer than 8 hydrogen bonds are the only molecules that may passively diffuse through the BBB. Due to the existence of tight junctions, passive paracellular transport of water-soluble substances is severely restricted in the BBB [52].

The BBB is equipped with a variety of different transporters to guarantee that crucial molecules may easily enter the brain to accommodate all the elements required to maintain brain homeostasis. These transporters may be divided into five more groups in addition to passive diffusion and transcellular transfer which are (i) active efflux transport, (ii) absorptive-mediated transport, (iii) carrier-mediated transport, (iv) ion transporters, and (v) receptor-mediated transport. In sum, the BBB plays a crucial role in the CNS's homeostasis and defense, and the treatment of CNS illnesses is therefore made more difficult since BBB restricts the crossover of medicines [52].

Given the properties of BBB, there are several challenges in the treatment of brain diseases. Its selective permeability restricts therapeutic efficacy and therefore it is necessary to study new drug delivery strategies to the brain, in order to provide an effective treatment [5]. Several strategies have been studied in this respect and are outlined in Table 1.

Table 1 - Drug delivery strategies to the brain.

Treatment	Strategy	Advantages	Disadvantages
Systemic Delivery	Receptor-targeting NPs	Minimally invasive Site-specific targeting	Low efficiency from BBB
Local Delivery	Intrathecal Delivery	Increased concentrations in CSF Bypass the BBB	Invasive High renewal of CSF
	Convection-enhanced delivery	Capacity to distribute a variety of drugs kinds Bypass BBB	Invasive
	Solid implant-based drug delivery	Brain surface delivery	Uneasy to refill the reservoir
	Nose-to-brain Delivery	Non-invasive Bypass the BBB	Hindered delivery efficiency due to mucociliary

NPs, as already mentioned, are becoming a popular choice for drug delivery due to their unique abilities, and one of them is to target specific areas of the body. Conjugating the NPs to a targeting moiety allows for better accumulation of DDS at tumor tissue, facilitates passage across BBB and enhances the effectiveness of treatment [53]. Some of the recently developed and studied brain delivery formulations for receptor-targeting NPs are transferrin (Tf), folate, and insulin-modified NPs since these receptors are overexpressed in the BBB [54].

Intrathecal (IT) administration is a local therapeutic strategy, where medications are directly injected into the cerebrospinal fluid (CSF). This method of delivery can maximize drug concentration at the CNS while minimizing off-target dosing and related effects. The subarachnoid area presents new obstacles to molecules that have been supplied by intrathecal injection, including intraventricular, intracisternal, or lumbar sites. As a result of the high rates of turnover as CSF clears, delivery of the medicines may be inadequate to tissue or cells [55].

Another approach for brain delivery is the convection-enhanced delivery (CED). CED uses a motor-driven pump to create an external pressure gradient and a microcatheter to administer the medication and induce fluid convection in the brain. Drugs can therefore reach the target tissue more efficiently than with the traditional local injection. Additionally, the drugs' molecular weight does not influence CED, and the diffusion is mostly affected by the pressure gradient. As a result, CED may be used to transport a variety of medications and the pressure gradient aids in preventing drug delivery backflow [56].

The idea behind solid implant-based delivery was to complement tumor resection surgery by directly implanting the material into the brain that acts as a medication reservoir. Because of this, the implant can be placed in the cavity without the need for extra surgery. Therefore,

this method offers the benefit of high medication delivery efficiency while minimizing the surgical burden [56]. The Gliadel Wafer containing carmustine is a prime illustration of a solid implant for GBM intracranial medication delivery. However, the wafer's shortcomings such as limited penetration, fast drug release, intracavity migration and drug resistance make it ineffective for treating GBM [57].

Intranasal administration is a successful and non-invasive method for delivering medications into the brain. The olfactory bulb, which is part of the CNS, serves as a distinctive structure that interfaces with the external environment. In nose-to-brain delivery, drugs can be transported directly to the brain via the olfactory or trigeminal nerves, as shown in Figure 4 [58]. By avoiding the liver's metabolism and reducing drug accumulation in non-target organs, nose-to-brain administration may effectively reduce systemic toxicity. This method has also gained popularity due to its various benefits, including its non-invasiveness, ease of use, and relatively quick adsorption [59].

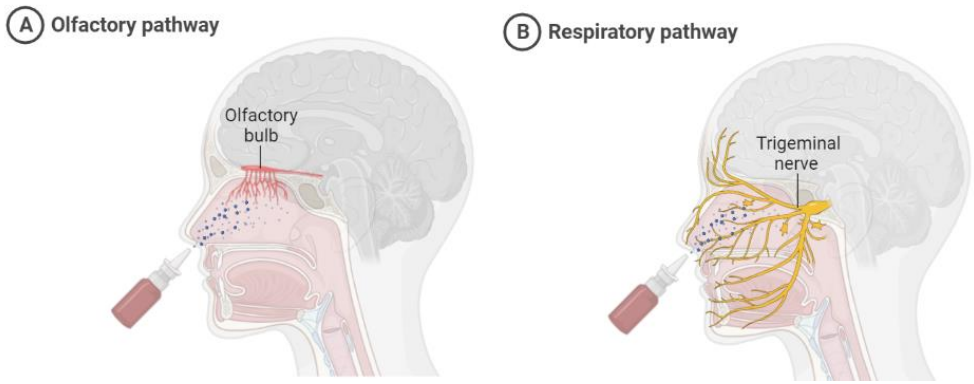

Figure 4 - Nose-to-brain delivery illustration.

Nevertheless, certain anatomical and physiological characteristics can pose significant limitations to this method of delivery. These include the high enzymatic activity within the mucus layer and the mucociliary clearance process occurring in the nasal cavity, which restricts intranasal absorption [54]. To overcome these challenges, NPs have been employed for intranasal drug delivery [60]. Various mucoadhesive polymers, such as CH, alginate, and cellulose, are employed to prolong the duration of adherence in the nasal cavity. Additionally, the use of positively charged NPs has shown promising results as they interact with the anionic mucin present in the nasal cavity [7].

2.3.2 - Drug Delivery Systems to incorporate Gemcitabine for the treatment of GBM

Several nanosystems have been evaluated and studied in their ability to incorporate GEM for the treatment of GBM. Different nanocarriers with different coatings have been explored and the main results of these studies are summarized in Table 2.

Table 2 - Nanosystems for the delivery of GEM for GBM therapy.

Nanocarrier	Coating	Targeting moiety	Size	Surface charge	Main conclusions	Ref.
Liposome	PEG	CD133 antibody	156 nm	negative	The use of PEGylated CD133-conjugated liposomes encapsulating GEM revealed an inhibition of GBM cells, both in vitro and in subcutaneous xenograft models of mice, a result of improved delivery of GEM, when compared with the free GEM.	[61]
Lipid Nanocapsules	n.a.	n.a.	n.d.	n.d.	The $GEMC_{12}$-LNC hydrogel delayed tumor recurrence in intratumoral glioma-bearing mice and rats. For the local treatment of GBM tumors, this hydrogel has proven to be an effective and secure technique.	[62][63]
Carbon Nitride Dots	n.a.	Transferrin	322.6 nm	negative	*In vitro* cytotoxicity studies have shown that the CN-GEM-Tf conjugation was able to cause apoptosis of pediatric GBM cells (SJGBM2) without affecting normal cells, up to a certain concentration.	[38]
PBCA NPs	Polysorbate-80	n.a.	112 nm	n.d.	GEM-PBCA-NPs have been demonstrated to efficiently inhibit intracranial tumor growth in rats and thus enhance the antitumor activity of GBM.	[64]

Gold NPs	PEG	n.a.	85 nm	positive	TMZ-GEM@PEG-AuNPs improved the synergic action of TMZ and GEM on the proliferation and toxicity of human GBM cells (U87).	[65]
Iron oxide NPs	HA	CTX	32 nm	neutral	IONP-HA-GEM-CTX *in vivo* studies proved to be able to cross the BBB in wild-type mice and showed prolonged blood circulation.	[66]
Squalene-based NPs	PEG	n.a.	90 – 150 nm	neutral	SQ-GEM-PEG NPs revealed a higher therapeutic efficacy when compared to free GEM in a rat bearing an orthotopic GBM tumor.	[67]

Abbreviations: Polyethylene Glycol (PEG), Glioma Stem Cell (GSC), Transferrin (Tf), Polybutylcyanoacrylate (PBCA), Chlorotoxin (CTX), Hyaluronic acid (HA), not applicable (n.a.), non-disclosed (n.d.).

Lipid-based NPs, such as liposomes, have been proposed for the encapsulation of GEM. Shin et al. (2014) selected PEGylated liposomes conjugated with an anti-CD133 monoclonal antibody (CD133-Ab) as a drug delivery carrier for GEM [61] since the transmembrane protein CD133 is overexpressed in GBM cells [68]. The results showed that the developed formulation displayed an extended circulation time due to PEGylation when compared with the free GEM, which was quickly eliminated from the bloodstream. Also, there was significant antitumor efficacy of this nanosystem in the subcutaneous mouse xenograft model, which resulted in greater regression of the average volume of the tumor. Additionally, in comparison to free GEM, the liposomes showed significantly less toxicity to the healthy organs. This study concluded that GEM was delivered more efficiently to tumor cells when the nanosystem is implemented [61].

Bastiancich et al (2018) developed a lipid nanocapsule (LNC) hydrogel for the encapsulation of a modified form of GEM, the lauroyl-gemcitabine. This LNC was composed of biodegradable, biocompatible and FDA-approved components [62]. This nanosystem was previously applied to mice [63] and the results showed that after administration of $GEMC_{12}$-LNC, there was an increase in survival rate when compared with the controls, as well as a delay in tumor recurrence. In the most recent study using rats, a delay in the formation of tumor recurrence was also found after the administration of $GEMC_{12}$-LNC into the resection cavity of glioma tumor-bearing rats. One week after implantation, $GEMC_{12}$-LNC hydrogel was still present in the resection cavity and the LNC's integrity was preserved during this time. This hydrogel proved to be a promising and safe tool for the local treatment of GBM tumors [62].

Carbon nitride dots (CNDs) are also suitable candidates for the incorporation of GEM. Liyanage et al. (2020) developed GEM-conjugate CNDs, with and without Tf for brain tumor targeting [38]. The developed nanoformulation CN-GEM-Tf caused apoptosis of pediatric GBM cells (SJGBM2) without affecting healthy human embryonic kidney cells (HEK293), at a maximum concentration of 10 nM, whereas CN-GEM required a 100-fold higher concentration. On the other hand, free GEM showed significant cytotoxicity towards the healthy cells. Using a zebrafish model, it was demonstrated that both CNDs and CN-GEM conjugate could pass the BBB, which further supports the potential of CNDs as a promising drug nanocarrier. This study demonstrated that this nanosystem was able to overcome the limitation of pediatric GBM chemotherapy such as non-specific targeting for the tumor cells as well as crossing BBB.

Wang et al. (2009) investigated the potential of PBCA NPs coated with polysorbate-80 for GEM encapsulation [64]. The authors study the *in vitro* antitumor effect of this nanosystem GEM-PBCA-NPs on C6 glioma cells, as well as it's *in vivo* pharmacodynamics in a model of rat intracranial brain tumor. This study demonstrated that this nanosystem could inhibit the proliferation of C6 glioma cells when compared to control NPs (without drug) and exhibit a higher cytotoxic effect when compared to free GEM. *In vivo*, GEM-PBCA-NPs could significantly extend the rat's survival compared with the saline control thus demonstrating their antitumor activity.

The suitability of gold NPs for GEM delivery has also been studied by Sahli et al. (2020). The authors have developed pegylated gold NPs based on TMZ complexes combined with GEM and

decitabine (DAC) [65]. DAC can significantly sensitize tumor cells to TMZ since it is responsible for regulating MGMT transcription. This work demonstrates that TMZ-GEM@PEG-AuNPs and TMZ-DAC@PEG-AuNPs can enhance the synergistic effect of decitabine and GEM with TMZ to target human GBM cells. The glycolysis pathway in U87 malignant glial cells was significantly affected, resulting in decreased lactate production in the culture medium. Tumor cells have as energy source the glycolytic metabolic pathway, and therefore a lower production of lactate (resulting product) is reflected in a lower available energy and therefore a decreased activity and progression of GBM. The complementary effect of these drugs was verified regarding increased toxicity and consequently decreased cell proliferation.

Mu et al (2015) developed iron oxide NPs for GEM delivery [66]. The nanocarrier was further modified with chlorotoxin (CTX) and hyaluronic acid (HA). HA was used to allow the conjugation of CTX peptide that is one of the most used target ligands for GBM since it has a high affinity for chloride channels and MMP-2 isoforms which are upregulated in GBM brain tissues [69]. The developed NPs, IONP-HA-GEM-CTX, showed a similar antiproliferative activity to free GEM in the two studied human GBM cell lines, SF-763 and U-118 MG. This means that GEM did not lose its antiproliferative activity, even after its conjugation onto the NPs' surface. Besides that, *in vivo* studies using wild-type mice proved that this nanosystem prolonged drug blood circulation and could successfully cross the BBB and reach the brain tissue [66].

Gaudin et al. (2016) developed squalene NPs for GEM delivery [67]. This nanosystem was coated with small percentages of PEG and was delivered by CED. In this research a chemotherapeutic study and a radiosensitization study were conducted with the SQ-GEM-PEG NPs and free GEM. The results demonstrated that the administration of the SQ-GEM-PEG NPs enhanced the therapeutic efficacy and increased survival of rats bearing orthotopic RG2 glioma tumors, when compared to free GEM used as a chemotherapeutic or as a radiosensitizer.

The present work aims to produce PLGA NPs functionalized with mucoadhesive polymer CH for the intranasal delivery of GEM to GBM therapy, given the ability of CH to adhere in the nasal cavity due to its positive charge. This nanosystem is an innovation since it is the first DDS designed for the nose-to-brain delivery of GEM.

Chapter 3

Materials and Methods

3.1 – Materials

Polyvinyl alcohol 4-88 (Mowiol ® 4-88, MW 31,000) (PVA), PLGA Resomer® RG 503 H (50:50; MW 24,000 – 38,000), Dichloromethane (MW 84.93; purity = 99%) (DCM), Acetic acid (≥ 98%, MW 60.05), phosphate-buffered saline (PBS), Sulforhodamine B (SRB) (MW 580.66), Trichloroacetic acid (TCA) (99%, MW 163.38) and Tris(hydroxymethyl)aminomethane (≥ 99.8%, MW 141.14) were acquired from Sigma Aldrich (St. Louis, MO, USA). Ethyl acetate (99.6%, ACS reagent, MW 88.11) (EA) was purchased from BioVision (Waltham, MA, EUA). Dimethyl sulfoxide (DMSO) (≥ 99.9%, MW 78.13) was purchased from VWR international (Radnor, PA, USA). Chitosan (MW 248 kDa, degree of diacylation 93) (CH) was obtained from Altakitin (Aveiro, PT). Gemcitabine hydrochloride (MW 299.66) was acquired from Med Chem Express (Monmouth Junction, NJ, USA). Trypsin (Gibco™ TrypLE™) and Fetal bovine serum (Gibco™ FBS) were obtained from Fisher Scientific (Hampton, NH, USA). From Capricorn Scientific (Ebsdorfergrund, Germany), high-glucose Dulbecco's Modified Eagle medium (DMEM) was bought. Trypan blue (≥ 70%, MW 960.80) was acquired from Biochem Chemopharma (Cosne-Cours-sur-Loire, France. Penicillin-Streptomycin solution (x100) was purchased from Biowest LCC (Riverside, MO, USA).

3.2 - Preparation of GEM loaded CH-PLGA NPs

GEM loaded CH-PLGA NPs were prepared using the double emulsion-solvent evaporation method. The results obtained from preliminary studies for the appropriate solvent choice, as GEM stability in water are presented in Appendix A3. The organic phase was first prepared, consisting of a known amount of PLGA in ethyl acetate (EA). Subsequently, a water-in-oil emulsion was prepared by adding a drop-by-drop solution of 1.0 mg of GEM in ultrapure water. Mechanical agitation of the two phases was performed using a vortex (Heidolph Reax Top Vortex

Mixer, Heidolph instruments GmbH & Co., Schwabach, Germany). To promote the formation of small droplets, the emulsion was submitted to 10 seconds on-off sonication cycles at an amplitude of 70% (UP400S ultrasonic processor, Hielscher, Berlin, Germany). The number of cycles of the sonication was varied in the different formulations as detailed in the next section.

Next, a solution of CH diluted in 60 µL of 1% acetic acid was prepared and mixed with a known concentration of polyvinyl alcohol (PVA). Then, this aqueous phase was added drop-by-drop to the previously prepared emulsion, yielding a water-in-oil-in-water emulsion. The w-o-w emulsion was then subjected to mechanical stirring and sonication steps as described above. The samples were kept in continuous stirring (Colosquid, ika®, magnetic stirrer) until complete evaporation of the organic solvent. The suspension of NPs was stored at 4 ºC to stabilize and prevent aggregation. Finally, the NPs were collected by centrifugation (MiniSpin®plus, Eppendorf, Germany) and resuspended in ultrapure water. Centrifugation was performed with successive increasing speeds and times. For the quantification of non-encapsulated drug, the supernatant was saved. Figure 5 shows an illustration of the procedure performed, respectively the realization of the double emulsion, as well as a schematic picture of the prepared NPs.

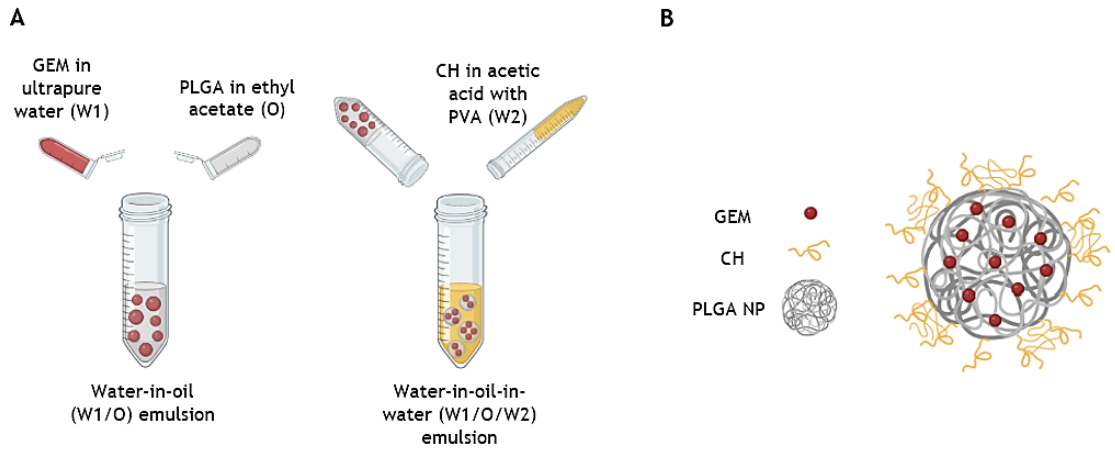

Figure 5 - (A) Schematic representation of the double emulsion method; (B) GEM loaded CH-PLGA NPs.

3.3 – Experimental Design and Protocol Optimization

To optimize the preparation protocol of the NPs, a design of experiments (DoE) was applied. The use of DoE in pharmaceutical products has been increasing in recent years, as it allows understanding the impact of input factors on their output responses, in a fast and rigorous way [70]. The application of this technique allows to simultaneously study the influence of several experimental parameters on the respective responses, through a small number of experiments.

In this work, a Central Composite Design (CCD) was implemented using the Design Expert software (13.0.5.0 version, Stat-Ease Inc., Minneapolis, USA). The CCD is the most widely used method in response surface modeling, due to the fact that it is more accurate and requires fewer experiments to build response models [71]. This model is based on the fractional factorial

design with center points (0), adding a group of axial points (α), which allows to estimate the curvature of the model. For that reason, in this second-order model, the factors are studied at five different levels (-α, -1, 0, +1, +α) [72]. Level -1 (low) represents the minimum value and level +1 (high) the maximum value of the parameter to be studied, both values previously defined by the experimental design developer. The design expert software automatically computed the α value (1.54671), after selecting a factorial orthogonal quadratic design. In Figure 6 is a representation of the CCD, where the positioning of the analyzed levels can be better understood.

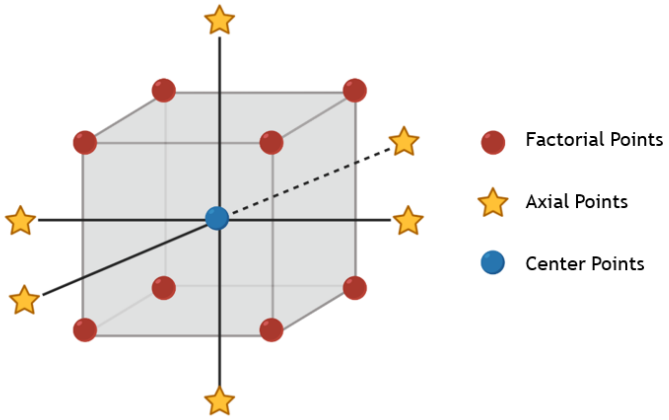

Figure 6 - Scheme of the CCD implemented.

The choice of the experimental parameters to be varied and their levels was based on preliminary studies. In those, only one parameter of the NPs preparation protocol was varied at a time. Thus, it was possible to conclude regarding the most important factors to vary in the preparation of the NPs and the most significant response characteristics to be analyzed. Thus, the CCD was then applied, choosing as the experimental variables the amount of PLGA, surfactant concentration, volume of solvents, and number of sonication cycles on the NPs' properties, as represented in Table 3.

Table 3 - Parameters of the Experimental Design.

Parameter	Units	Applied level					Responses	Units
		-α	- 1	0	+ 1	+ α		
m_{PLGA}	mg	1.8	10.0	25.0	40.0	48.2	**Size**	nm
$\%_{PVA}$	% (w/v)	0.2	1.0	2.5	4.0	4.8	**PDI**	-
V_{EA}	µL	90	500	1250	2000	2410	**Zeta potential**	mV
Sonication Cycles	unit	0.9	2.0	4.0	6.0	7.1	**EE**	%

Note: m_{PLGA} - PLGA mass; $\%_{PVA}$ – percentage of PVA; V_{EA} – volume of Ethyl Acetate; Sonication Cycles – number of sonication cycles of 10 seconds each.

The analyzed responses were the size of the NPs, PDI, zeta potential and GEM encapsulation efficiency (EE). 27 independent formulations were produced, in which there are 3 replicates of

the center points of each variable. Table 4 provides a summary of the experimental plan and results.

Table 4 - Overview and outcomes of the experimental plan.

Run Order	Independent Variables				Dependent Variables			
	m_{PLGA}	$\%_{PVA}$	V_{EA}	Sonication cycles	Size (nm)	PDI	Zeta Potential (mV)	EE (%)
1	-1	-1	-1	-1	166.4	0.191	36.2	33.5
2	+1	-1	-1	-1	254.7	0.21	26.8	33.8
3	-1	+1	-1	-1	161.6	0.253	25.1	28.5
4	+1	+1	-1	-1	165.4	0.148	11.8	26.5
5	-1	-1	+1	-1	169.7	0.159	18.6	1.8
6	+1	-1	+1	-1	207.5	0.19	19.4	13.0
7	-1	+1	+1	-1	180.4	0.185	18.6	37.8
8	+1	+1	+1	-1	194.5	0.236	22.8	31.4
9	-1	-1	-1	+1	156.7	0.156	23.1	35.6
10	+1	-1	-1	+1	233.2	0.112	24.3	33.4
11	-1	+1	-1	+1	142.9	0.199	12.9	41.8
12	+1	+1	-1	+1	155.4	0.134	13.0	25.5
13	-1	-1	+1	+1	169.5	0.154	23.9	19.7
14	+1	-1	+1	+1	168.6	0.115	16.9	21.9
15	-1	+1	+1	+1	147.1	0.194	11.4	34.3
16	+1	+1	+1	+1	200.9	0.334	10.1	37.3
17	-α	0	0	0	193.6	0.476	15.7	25.3
18	+α	0	0	0	218.4	0.217	13.3	26.0
19	0	-α	0	0	418.5	0.076	26.3	14.6
20	0	+α	0	0	163.9	0.157	14.4	24.6
21	0	0	-α	0	878.8	0.258	51.4	37.7
22	0	0	+α	0	184.1	0.243	21.8	34.3
23	0	0	0	-α	236.0	0.245	15.4	20.1
24	0	0	0	+α	195.7	0.221	20.7	30.3
25	0	0	0	0	166.5	0.135	21.3	31.3
26	0	0	0	0	162.7	0.175	20.5	30.2
27	0	0	0	0	155.3	0.101	20.5	25.7

Each response variable was individually fitted to the mathematical regression model, represented below [71]. In this polynomial regression, a relationship is established between the different experimental parameters and each response studied.

$$Y = b_0 + b_1X_1 + \cdots + b_kX_k + b_{12}X_1X_2 + b_{13}X_1X_3 + \cdots + b_{k-1,k}X_{k-1}X_k + b_{11}X_1^2 + \cdots + b_{kk}X_k^2 + \epsilon \quad (1)$$

Within this equation, Y represents the dependent variables (outcome variables), X_k denotes the independent variables, b_0 signifies the overall mean response (intercept constant), while b_k stands for the coefficients in the regression model. K represents the number of independent variables, and ϵ represents the error term.

Statistical analysis (ANOVA) was then used to determine the optimal experimental conditions to produce optimized NPs with suitable features for nose-to-brain delivery (size below 200 nm, low PDI values and positive zeta potentials). At a 95% confidence level, p-values less than 0.05 were considered significant.

3.4 - NPs Physicochemical Characterization

The physicochemical characterization of NPs was based on size (nm), PDI, and zeta potential (mV) measurements. For this purpose, it was used the technique of Dynamic Light Scattering coupled with Laser Doppler Electrophoresis. To perform this technique, a ZetaSizer Nano ZS equipment (Malvern Instruments, UK) was used, and the data obtained were analyzed by ZetaSizer software (version 8, Malvern).

3.4.1 - Dynamic Light Scattering

The Dynamic Laser Scattering (DLS) technique is a well-established and non-invasive methodology for measuring the size and size distribution of molecules and particles that have been dispersed in a liquid. A beam of light hits the sample, and the Brownian motion of these particles, which is the random motion of the particles suspended in the fluid, causes the laser light to be scattered with different intensities. The analysis of these intensity fluctuations allows the determination of the Brownian motion speed which is quantified as the Translational Diffusion Coefficient (*D*). For a constant temperature and a known dispersant viscosity, the size of the NPs can be determined via the hydrodynamic radius (R_H) by applying the Stokes-Einstein equation, as represented below [73].

$$R_H = \frac{kT}{6\pi\eta \mathrm{D}} \quad (2)$$

Where *T* is the absolute temperature, *η* the solvent viscosity of the medium, *k* is the Boltzmann constant, and *D* is the diffusion coefficient. The hydrodynamic radius consists of the radius of a sphere that diffuses with the same coefficient/rate as the particle being measured. This sphere consists of the central particle plus its solvation shell. For this reason, the hydrodynamic radius is larger than the actual radius of the NP [73].

The DLS technique also measures other parameters such as PDI. The PDI evaluates the particle size distribution and is used to describe the degree of homogeneity of a suspension [74]. For a monodisperse sample, its PDI is expected to be less than 0.20 [75].

For the measurement of the hydrodynamic diameter, a standard cell (Sarstedt®) made of polystyrene was employed and a dilution in ultrapure water (1:10) was performed for a final concentration of NPs of 1.0 mg/mL. The refractive index of water as the dispersant at 25 ºC was set to 1.330, while the viscosity was set to 0.8872 cP. The polymer refractive index was fixed at 1.59, and the absorption was set at 0.01.

3.4.2 - Laser Doppler Velocimetry

When DLS is associated with Laser Doppler Electrophoresis, it is possible the determination of the zeta potential. The zeta potential is a measure of the magnitude of repulsion or electrostatic attraction, being one of the parameters that affect the stability of colloidal dispersions. When a charged particle is suspended in a liquid, a double layer consisting of ions/molecules is adsorbed on its surface. This double layer is formed by the Stern layer, composed of ions of opposite charge to the particle, and the diffuse layer, in which the ions move more freely. The slipping plane is at the end of the diffuse layer and marks the end of this double layer [76].

The zeta potential, often represented by ζ, consists of the potential measured in the slipping plane, which separates the mobile fluid from the stationary layer of the fluid, attached to the surface, as represented in figure 7 [76].

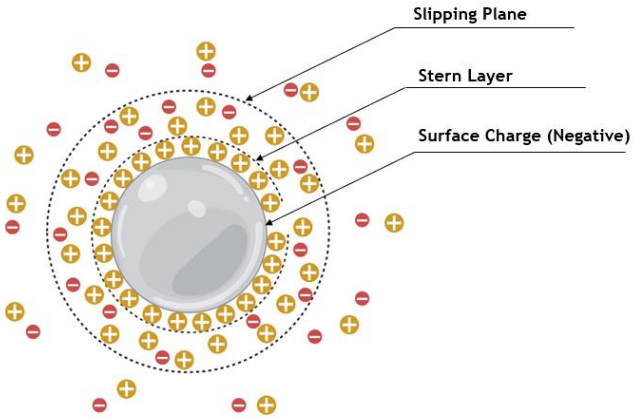

Figure 7 - Representation of the layers concerned in zeta potential measurement.

When a sample is subjected to an electric field, the particles move towards the oppositely charged electrode. This effect is called electrophoresis and it is based on it that the zeta potential is measured. Therefore, as it is not possible to measure the zeta potential directly, an electric field is applied to the sample, thus determining the electrophoretic mobility of the particles, represented by μ_e. This property can be obtained through the equation shown below, when the values of particle velocity (v) and induced electric field (E) are already known [77].

$$\mu_e = \frac{v}{E} \tag{3}$$

The zeta potential is obtained through the value of the electrophoretic mobility calculated previously, using Henry's equation:

$$\mu_e = \frac{2\varepsilon_r \varepsilon_0 \zeta f(\mathrm{Ka})}{3\eta} \tag{4}$$

Where ε_r represents the relative permittivity or dielectric constant, ε_0 the permittivity in vacuum, ζ the zeta potential, *f(Ka)* the Henry's function and *η* the viscosity of the medium at the temperature at which the measurement is being carried out [77].

For the zeta potential analysis of the NPs, a DST1060 cell (Malvern Panalytical) containing two gold-plated beryllium electrodes was used, to generate the electric field necessary for its determination. A dilution in ultrapure water (1:10) was also performed for a final concentration of NPs of 1.0 mg/mL. The ZetaSizer software conducted three measurements for each sample using the Smoluchowski model. The measurements used the dielectric constant and the viscosity of water, respectively with the values 78.5 and 0.8872 cP.

3.5 - Determination of the Encapsulation Efficiency

The encapsulation efficiency (EE) of GEM in the prepared NPs was determined indirectly by quantifying the non-encapsulated drug in the supernatant, by UV-Vis spectrophotometry. This non-invasive technique allows the quantification of absorbed light as a function of wavelength. Radiation is transmitted and absorbed in varying degrees as it moves through the sample and a detector receives the radiation that was sent. The Lambert-Beer law shows the linear relationship between the concentration of a sample and its absorbance and is used to calculate the numerical value in a UV-Vis spectroscopy experiment, as shown in the equation below [78].

$$A = \varepsilon\, c\, d = -\log\left(\frac{I}{I_0}\right) \tag{5}$$

Where, *A* is the absorbance; ε is the molar absorption coefficient, c is the concentration; d is the path length of the measuring beam in the sample; *I* is the light that reached the detector (the intensity of the measuring beam after passing through the sample); I_0 is the intensity of the measuring beam before passing through the sample.

The free GEM was quantified by UV-Vis absorbance measurements (Synergy 2 Microplate Reader, BioTek, UK) at λ_{max} 268 nm and correlated to GEM calibration curve in PVA (figure A1 in appendix A). The EE values for GEM were determined using the following equation:

$$EE(\%) = \frac{total\ amount\ of\ drug - amount\ of\ free\ drug}{total\ amount\ of\ drug}\ x\ 100 \quad (6)$$

3.6 - Fourier Transformed Infrared Spectroscopy

Fourier-Transformed Infrared Spectroscopy (FTIR) has been used to characterize molecular structures. This technique allows the analysis of chemical compositions by accurately detecting molecular conformations, such as functional groups, bond types and molecular interactions present in the sample [79].

In FTIR the sample is exposed to an infrared light, some of which is absorbed and part of which goes through. The sample converts the energy received from the radiation into vibrational or rotational energy, creating a signal. The final signal produced at the detector is a spectrum that shows the molecular signature of the sample, with the absorption peaks represented. Each molecule has a unique spectrum, since it has specific chemical bonds, which makes FTIR an important instrument for chemical identification. The resultant spectrum is provided as absorbance/transmittance vs. 1/wavelength, commonly known as wavenumber (cm^{-1}) [80].

This technique has several advantages of which include simplicity, being a fast, non-destructive and reagent free analytical tool. Furthermore, it only requires a small quantity of samples, in the nanogram to microgram range [81] .

A Bruker Alpha-P FT-IR Spectrometer (Bruker Optics Inc., Billerica, MA, USA) and Opus Software (version 6.5, Bruker Optik GmbH) were used to record the FTIR spectra of the produced NPs. A 10 µL drop of each sample containing the NPs was directly deposited into the ATR crystal, and it was then dried with a nitrogen flow. The spectra were captured in absorbance mode with 64 scans at a resolution of 4 cm^{-1} for both the sample and background observations, and a wavenumber range of 4000-375 cm^{-1}. The FTIR measurements were performed for PLGA NPs, CH-GEM-PLGA NPs, CH and GEM. The spectra analysis was performed in GraphPad Prism (version 9.1.2, GraphPad Software, USA).

3.7 – Transmission electron microscopy

Transmission electron microscopy (TEM) is a potent imaging method that produces high-resolution pictures of exceedingly small objects or thin materials using an electron beam. Using TEM, scientists and researchers may see the precise shape, structure, and composition of materials down to the atomic or nanoscale [82]. A thin specimen is passed through by an electron beam in a TEM, where the electrons interact with the material and scatter as a result. Then, a collection of the dispersed electrons is utilized to create a picture [83]. Different sorts of information, including bright-field imaging, dark-field imaging, high-resolution imaging, diffraction patterns, and elemental mapping, may be acquired by modulating the electron beam and utilizing different detectors [84].

Since light atoms make up biological material, very small density fluctuations should be amplified to provide a discernible contrast in electron micrographs. Heavy metals are typically used as a staining agent to achieve this. Due to its inexpensive cost, the exceptional contrast it offers, and its natural affinity for biological materials, uranyl acetate solution has long been regarded as the gold standard [85]. The study of nanomedicine has made extensive use of this microscopy technology [84].

For visualization of the NPs by TEM technique, 5 µL of the suspension of the prepared NPs were placed on a copper grid (Formvar/Carbon - 400 mesh Copper, Agar Scientific, UK) for 5 minutes. After removing the excess liquid from the grid, the NPs embedded in the grid were stained with 2% (v/v) uranyl for 45 seconds. After that time, the excess uranyl was removed from the grid and went through the same process again, this time it was immediately removed. At least three images per sample were acquired at an accelerating voltage of 80 kV using a Jeol JEM 1400 electron microscope (Japan).

3.8 - *in vitro* Release of GEM from the CH-PLGA NPs

in vitro studies were conducted to evaluate the controlled release of GEM from CH-PLGA NPs. These studies were performed under simulated physiological conditions, for which the NPs were suspended in phosphate-buffered saline (PBS) (0.01 M) and kept at 37°C, under continuous stirring. PBS allows to simulate human body conditions, such as the ionic strength and pH of blood and tissues [86]. To do this, the study of drug release was done in two different PBS pHs, pH 6.4 and pH 7.4, in order to simulate the pH of tumor tissues and blood/healthy body tissues, respectively [87].

To better simulate the tumor environment, the lysozyme was added at a concentration of 1.0 mg/mL to the PBS medium (pH 6.4). Lysozyme is available in the human body in almost all fluids, but is reported to be overexpressed in the CSF of GBM patients [88]. This enzyme promotes the degradation of CH, that forms a layer on the NPs' surface [89].

For the experiments, the NPs' samples were divided in 10 aliquots, and the amount of drug released from the aliquots was measured over time, at previously determined times. For this, it was proceeded at each timepoint, the centrifugation of the aliquot, in order to separate the NPs from the supernatant. The amount of released GEM was determined through the supernatant, by UV-Vis absorbance. To establish a relationship between the measured absorbance and the amount of drug, calibration curves of GEM in PBS were plotted for the different pH used (Figure A1.2 and A1.3 in appendix A). The percentage of drug released as a function of time, is given by the following equation:

$$\%\ Drug_{release} = \frac{amount\ of\ drug\ released\ at\ time\ t}{amount\ of\ encapsulated\ drug} \times 100 \quad (7)$$

3.9 – Evaluation of NPs' stability

The stability of GEM-loaded CH-PLGA NPs was studied by DLS measurements, analyzing the variations in size, PDI and zeta potential over time. This stability was analyzed under storage and physiological conditions.

Regarding storage conditions, NPs were stored in ultrapure water at three different temperatures, 4°C, room temperature and at 37°C. Concerning physiological conditions, the prepared NPs were suspended in PBS with three different pHs (pH 5.8, pH 6.4 and pH 7.4) and stored at 37°C. The stability of the NPs in PBS (pH 5.8) was studied since this is the degree of acidity of the nasal mucosa [90]. As the NPs are intended to be delivered to the brain intranasally, the study of their stability under these conditions is relevant.

3.10 – Cells and cell culture

Two distinct human GBM cell lines were used to perform the cellular tests and evaluate the cytotoxicity of the prepared NPs. The cell lines were U251 and T98G, with different MGMT expression. The U251 cell line shows a lack of functional MGMT expression, which gives it a high sensitivity to the effect of alkylating agents [91]. The T98G cell line shows a functional expression of the MGMT enzyme. Because there is MGMT activity, these cells are more resistant to treatment with alkylating agents [92].

Both cell lines were grown in DMEM, which was supplemented with 10% FBS. 1% penicillin-streptomycin and 1% fungizone were added to the medium to prevent contamination in the cell culture. The cells were detached using trypsin and passaged when they reached an approximate confluence of 80%. Throughout the entire experimental process, the cultures were consistently maintained at 37°C in a 5% CO2 incubator.

3.11 - Sulforhodamine B assay

U251 and T98G cell lines were used to evaluate the inhibitory effects on cell survival of free GEM, GEM-loaded CH-PLGA NPs and CH-PLGA NPs. A Sulforhodamine B (SRB) colorimetric test was used for this study. This method assesses the concentration of cellular proteins and is directly related to cell survival and proliferation [93].

The cells were seeded at a density of 1,000 cells per well in 96-well plates and allowed to adhere for 24 hours at 37 ºC in a humidified 5% CO2 incubator. Free GEM, GEM-loaded CH-PLGA NPs, and CH-PLGA NPs were then diluted in DMEM media and distributed to the cells. The negative control cells were those that received no treatment. The SRB technique was carried out after a 72-hour incubation period. The cells were first fixed with 10% (w/v) trichloroacetic acid (TCA) at 4ºC for 1 hour, then washed and air-dried at 37 ºC. After that, 50 µL of SRB was applied to each well, and the staining process took 20 minutes. The samples were washed twice with 1% (v/v) acetic acid to eliminate unbound SRB and dried at 37ºC. By adding 100 µL of Tris

buffer solution, the protein-bound stain was solubilized for UV-Vis absorbance measurements. A BioTek Synergy HT Microplate Reader (BioTek, UK) was used to quantify the protein concentration at 560 and 655 nm. Cell proliferation was assessed using the following mathematical expression.

$$Cell\ survival\ \ (\%) = \frac{T}{C}\ x\ 100 \tag{8}$$

In this equation, T represents the absorbance values measured in the wells with treated cells at the end of the incubation period, while C represents the absorbance values measured in the wells containing untreated cells (control).

3.12 - Statistical analysis

The statistical analysis was performed using the Student's t-test with a 95% confidence interval. A p-value of less than 0.05 was considered statistically significant. This test was used for the stability measurements of the prepared NPs as well for the cell experiments.

Chapter 4

Results and Discussion

4.1 - Experimental Design and Protocol Optimization

The implementation of DoE allowed a faster and more efficient optimization of the NPs preparation protocol. For this, as mentioned in chapter 3.3, the independent variables selected were the mass of PLGA, the concentration of PVA, the volume of ethyl acetate, and the number of sonication cycles. By varying these parameters, it was possible to study their effect on the chosen dependent variables: the size of the NPs, PDI, zeta potential, and EE of the GEM.

ANOVA statistical analysis found that the model was significant for all variables under study ($p<0.05$), except for the PDI ($p>0.05$) that for this reason was not considered for the model. The statistical analysis results are summarized in Table 5 and expanded in Tables A2.1-A2.4 in Appendix 2. Thus, the CCD allowed for a significant study of the variable's size and zeta potential, which were fitted to a quartic regression model, and the EE variable, that was fitted to a quadratic regression model.

Table 5 - Results of ANOVA statistical analysis for the significant variables (size, zeta potential and EE)

Parameter			**Size**		
	SS	dF	MS	F-Value	p-value
Model	$5.299x10^5$	24	22079.11	680.61	0.0015
Residual					
Lack of Fit					
Pure Error	64.88	2	32.44		
Cor Total	$5.300x10^5$	26			
R^2			0.9999		

Parameter	Zeta Potential				
	SS	dF	MS	F-Value	p-value
Model	1875.67	24	78.15	366.34	0.0027
Residual					
Lack of Fit					
Pure Error	0.4267	2	0.2133		
Cor Total	1876.10	26			
R^2			0.9998		
Parameter	**EE**				
	SS	dF	MS	F-Value	p-value
Model	1795.05	14	128.22	6.66	0.0011
Residual	231.18	12	19.26		
Lack of Fit	213.57	10	21.36	2.43	0.3271
Pure Error	17.61	2	8.80		
Cor Total	2026.23	26			
R^2			0.8859		

Abbreviations: sum of squares (SS); mean square (MS).

The regression model has a good fit for the response prediction regarding size, zeta potential, and EE, as shown in Table 5. Figure 8 shows the graphs between the experimental values obtained and the predicted values for each of the significant variables.

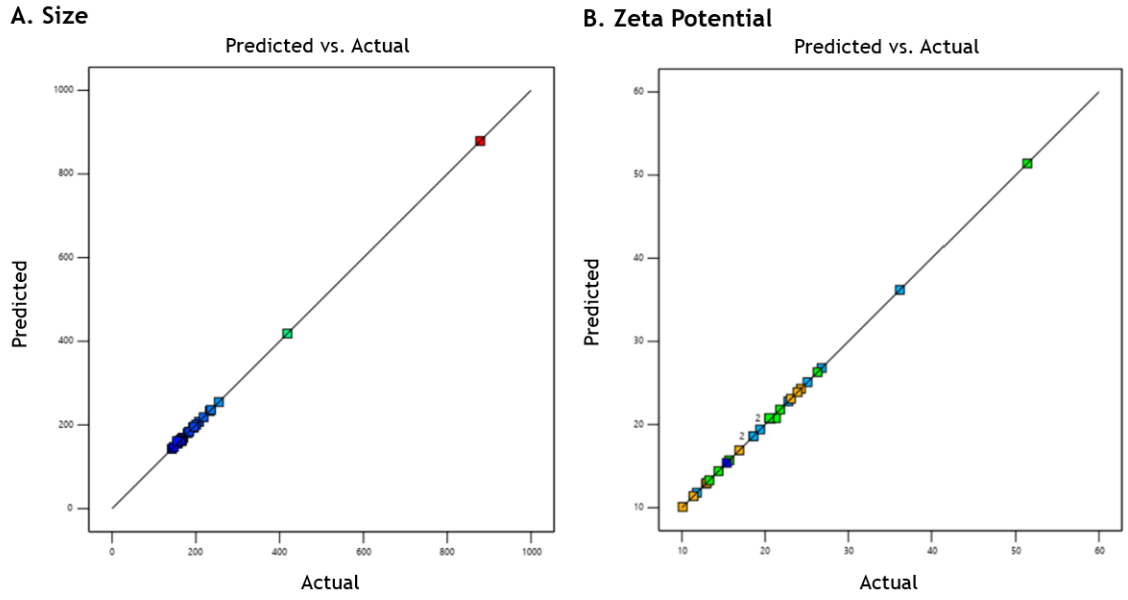

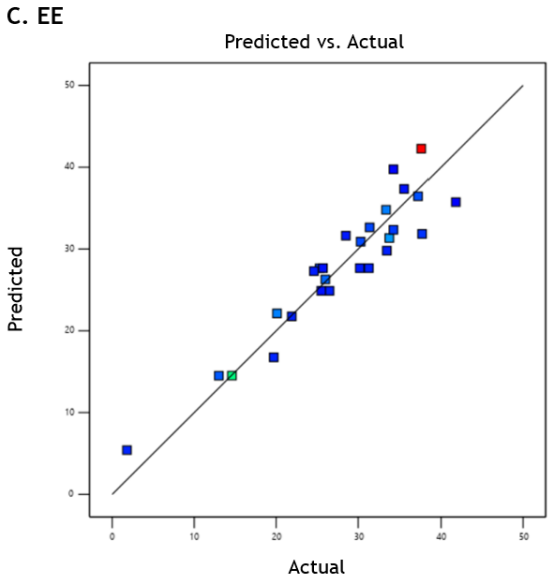

Figure 8 - Plots between the experimental values obtained and the predicted values for the significant variables (A) Size, (B) Zeta Potential and (C) EE.

Through Figure 8 it is possible to observe that there is a good agreement between the predicted and the obtained experimental values, for the three variables. Regarding Figure 8(A) and (B), which analyze the values of size and zeta potential, the agreement is practically total, which would be expected by the high value of R^2 in both ($R^2 = 0.999$), as recorded in Table 5. In the case of the EE variable, there is a good agreement but with some values slightly different from those predicted, which is justified by the R^2 value that is lower than the variables previously analyzed ($R^2 = 0.886$).

Regression coefficients (RC) were determined for the significant variables. The RCs describe the effect that changing these variables causes on the responses under study. A positive RC reflects a positive effect on that response: that is, an increase in the response. While a negative sign has the opposite impact, meaning that increasing this variable causes a decrease in the response. The response equation for each variable was obtained through the RC, and only the significant terms were considered ($p<0.05$). The equations for the variables size, zeta potential and EE are in Appendix 2, with the respective numbers A2.5, A2.6, and A2.7.

4.1.1- Influence on the NPs' Size

The *in vivo* behavior of NPs is significantly influenced by their size. Size directly affects various factors, including the half-life of NPs and their biodistribution [94]. Larger NPs can initiate distinct biological processes such as macrophage uptake and circulation arrest [95]. The permeation and retention of the NPs inside the tumor is limited by the fenestrations present in the tumor vessels, which typically range between 200 and 800 nm. For this reason, it is important to ensure that their size does not exceed 200 nm [96].

The NPs synthesized in CCD showed a size distribution ranging from 142.9 nm (formulation 11) to 878.8 nm (formulation 21), as described in Table 4. Visual representations in the form of

2D contour plots and 3D response surface plots, represented in Figures 9 and 10, respectively, show the impact of several independent variables on the size of the NPs.

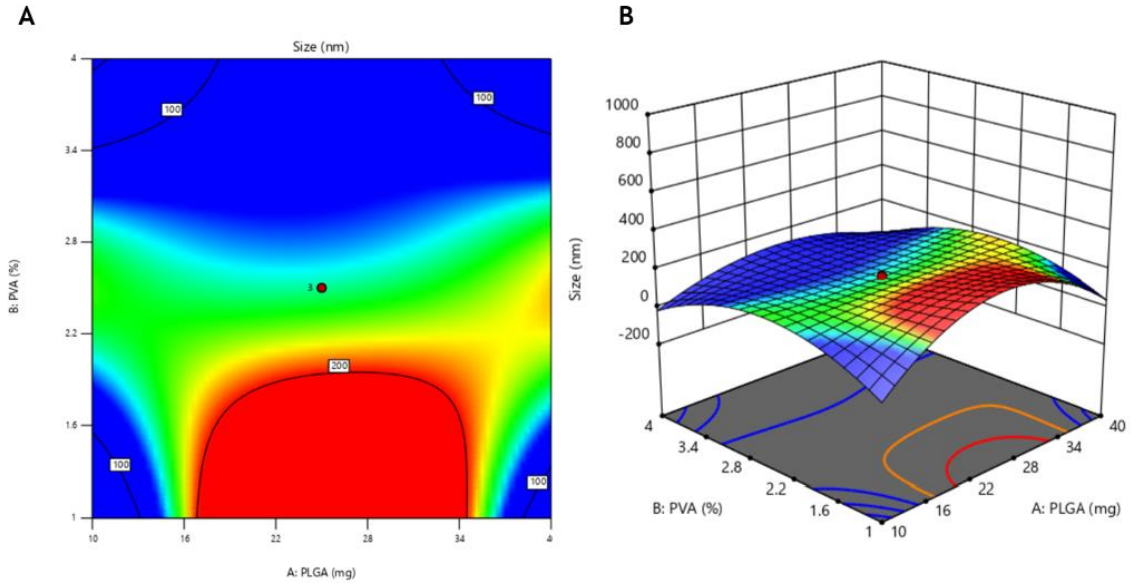

Figure 9 - (A) 2D contour plot and (B) 3D response surface plot displaying the impact of PLGA mass and the %PVA, on the NP size. The blue color represents smaller sizes of NPs and the red color represents larger sizes of NPs.

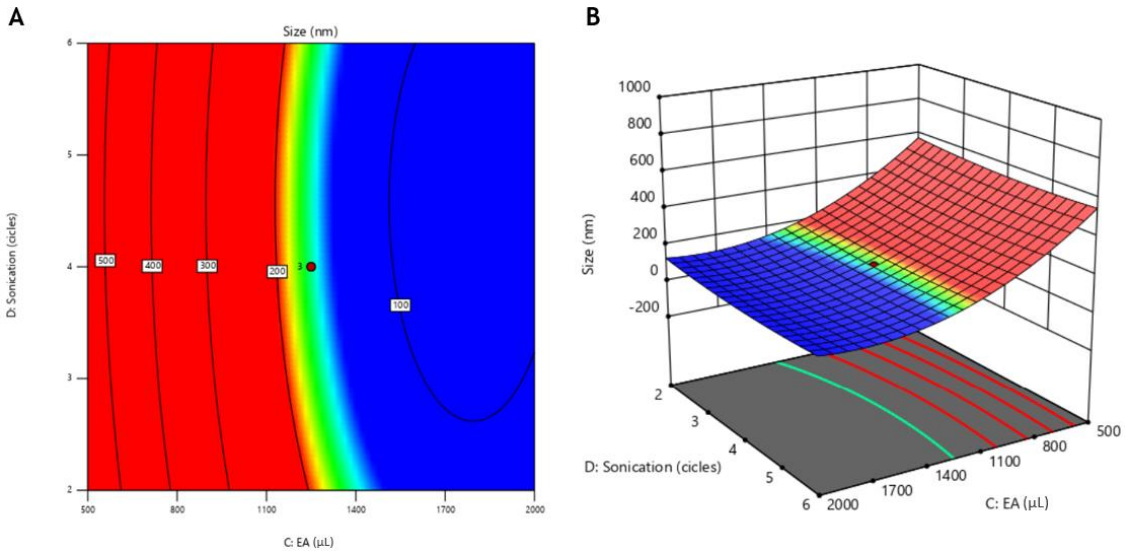

Figure 10 – (A) 2D contour plot and (B) 3D response surface plot displaying the impact of EA volume and the number of sonication cycles on the NP size. The blue color represents smaller sizes of NPs and the red color represents larger sizes of NPs.

By examining the RC values of the regression equation (eq. A2.5, appendix A2), it can be concluded that the mass of PLGA positively influences the size of the NPs. A higher quantity of PLGA results in the formation of larger NPs. This phenomenon occurs because an increased concentration of the polymer elevates the viscosity of the organic phase. Consequently, the diffusion of the organic solvent into the aqueous phase is difficulted, leading to the formation of larger oil droplets during the emulsification process [97]. In contrast, the volume of EA shows a negative influence, meaning that the smaller the volume of ethyl acetate the larger the size

of the NPs. This happens for the same reason as the increase in viscosity of the organic phase, explained previously.

The concentration of PVA and the number of sonication cycles exhibited a negative influence on the size of NPs. Consequently, increasing these variables led to the formation of smaller NPs. PVA plays a role in stabilizing the emulsion through steric effects, which diminishes the interfacial tension between the oil droplets containing PLGA and the surrounding aqueous phase [98]. Furthermore, the sonication cycles allow the emulsion droplets to be broken down into smaller droplets. Therefore, for a larger number of sonication cycles performed NPs with smaller sizes will be produced [99].

4.1.2- Influence on the NPs' Zeta Potential

The zeta potential is positive for all NPs, which proves the presence of the cationic amino groups of the chitosan on the surface of the NPs. Since, in the absence of CH, the PLGA NPs would have a negative zeta potential due to the existence of the carboxylic terminal groups of PLGA [100]. CH was chosen for the NPs coating due to being positively charged, therefore allowing interaction with the negatively charged mucin of the nasal mucosa, which may lead to an enhanced brain delivery [101]. Furthermore, the surface characteristics of NPs give indications concerning their stability. A higher magnitude of the zeta potential indicates greater *in vitro* stability of the NPs. This is due to the fact that a stronger repulsive force is present and therefore prevents the particles from getting close to each other, consequently hindering the formation of aggregates [102].

The produced NPs showed a zeta potential distribution ranging from 10.1 mV (formulation 16) to 51.4 mV (formulation 21), as described in Table 4. Visual representations in the form of 2D contour plots and 3D response surface plots, represented in Figures 11 and 12, show the influence of several independent variables on the zeta potential of the NPs.

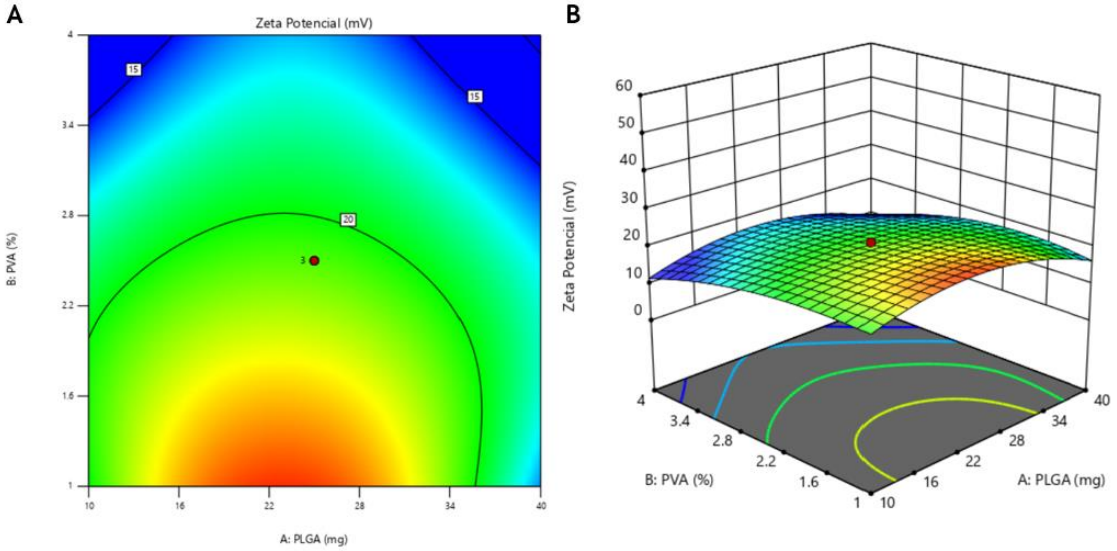

Figure 11 - (A) 2D contour plot and (B) 3D response surface plot displaying the impact of PLGA mass and the %PVA, on the NP zeta potential. The blue color represents lower zeta potentials and the red color represents higher zeta potentials.

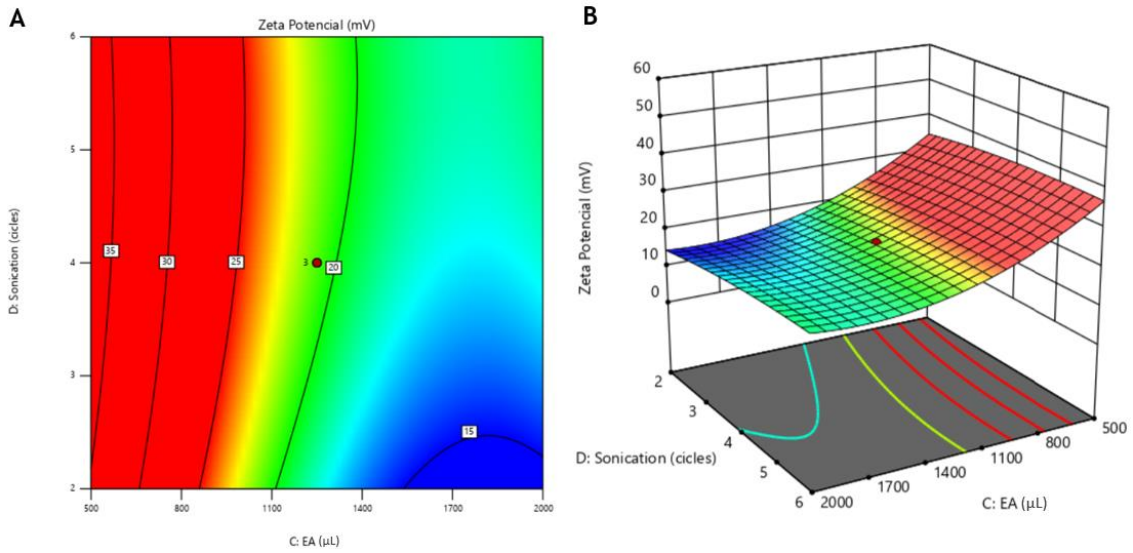

Figure 12 - (A) 2D contour plot and (B) 3D response surface plot displaying the impact of EA volume and the number of sonication cycles, on the NP zeta potential. The blue color represents lower zeta potentials and the red color represents higher zeta potentials.

Using the regression equation (eq. A2.6, Appendix A2), it can be concluded that the mass of PLGA, the percentage of PVA and the volume of EA negatively influence the zeta potential of the NPs. An increase in these variables results in a decrease in zeta potential. On the contrary, the number of sonication cycles has a positive effect on the zeta potential. The increase in sonication cycles/time contributes to smaller particle size and a narrower size distribution. This phenomenon can be attributed to the larger surface area of the smaller particles, which results in a more pronounced positive charge [103].

4.1.3- Influence on the NPs' EE

The prepared NPs presented an EE distribution ranging from 1.8% (formulation 5) to 41.8% (formulation 11), as described in Table 4. Visual representations in the form of 2D contour plots and 3D response surface plots, represented in Figures 13 and 14, show the effect of several independent variables on the EE of the NPs.

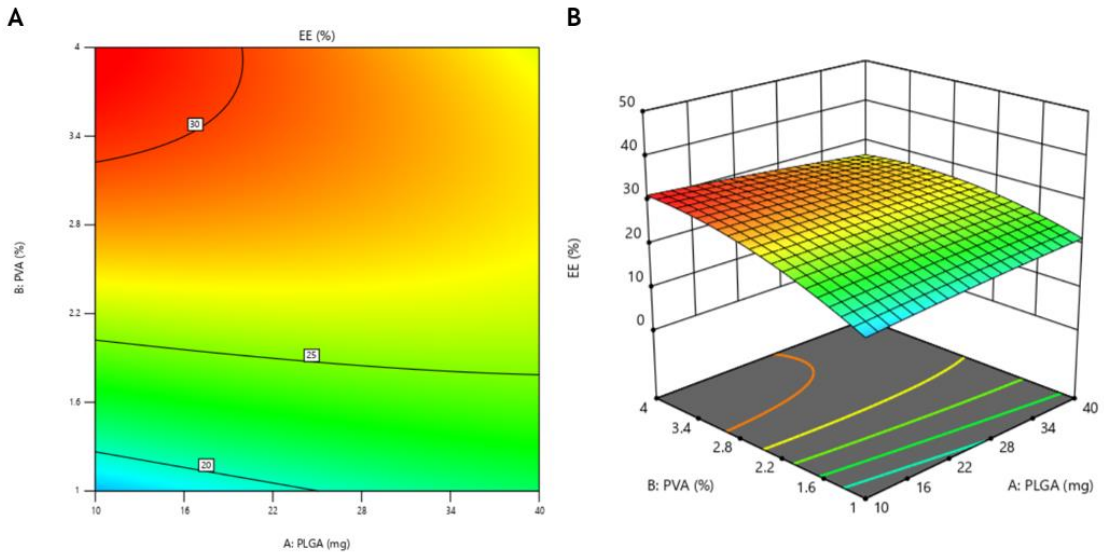

Figure 13 - (A) 2D contour plot and (B) 3D response surface plot displaying the impact of PLGA mass and the %PVA, on the EE of the NP. The blue color represents lower EE and the red color represents higher EE.

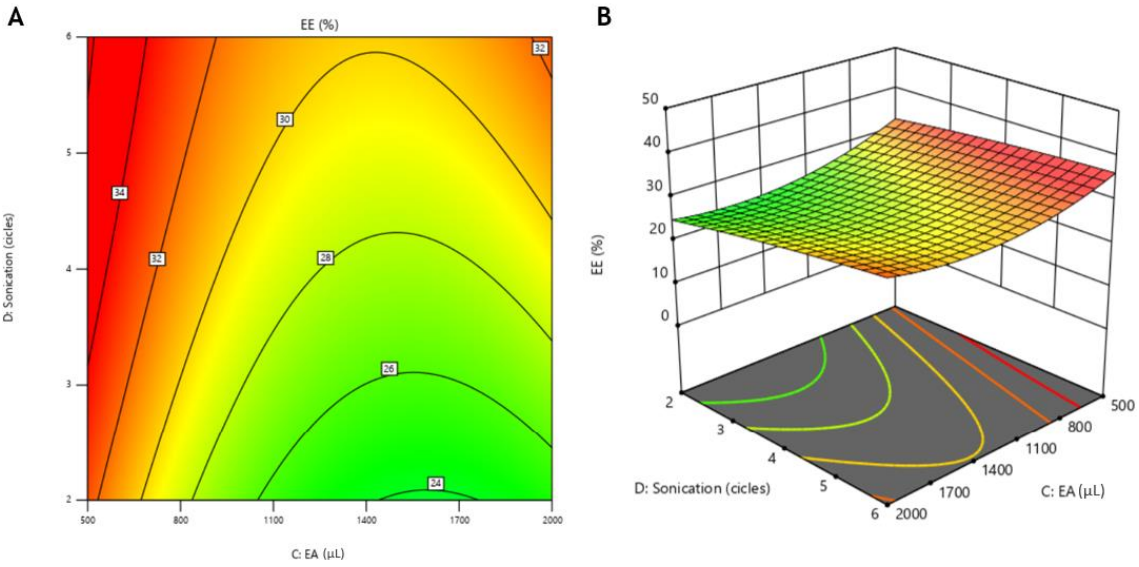

Figure 14 - (A) 2D contour plot and (B) 3D response surface plot displaying the impact of EA volume and the number of sonication cycles, on the EE of the NP. The green color represents lower EE and the red color represents higher EE.

By analyzing the regression equation (eq. A2.7, Appendix A2), it can be concluded that PLGA mass and EA volume negatively influence the EE of the NPs. A decrease in the volume of EA generates a higher EE, since the increased viscosity of the organic phase can generate a greater resistance to diffusion of the drug into the outer aqueous phase, which leads to a higher imprisonment of the drug in the NPs [103].

On the other hand, the percentage of PVA and the number of sonication cycles positively affect the EE. As the surfactant affects the interface through which the drug passes, changes in PVA concentration imply changes in the concentrations of the drug between the two phases. The use of an optimal surfactant concentration influences the diffusion of the drug through the water/oil interface, thus leading to an increase in the EE [104]. More cycles of sonication can lead to a decrease in the diffusion of the drug into the outer aqueous phase, moreover it can

cause faster hardening of the PLGA, since a quicker loss of the oily phase occurs due to faster evaporation, leading to a higher EE [105]. Also, increasing the number of sonication cycles/time of sonication causes the creation of monodisperse small particles, which exhibit greater efficiency in encapsulating the drug compared to polydisperse larger particles [103].

4.2 – Data Optimization and Model Validation

Optimization of the protocol was done after the limits of each response were established. Regarding the size of the NPs, this was set between 160-200 nm, the zeta potential between 15-30 mV, and the EE between 30-100% (with the aim to maximize). The software predicted the levels for each independent variable to meet the chosen response specifications, as represented in Table 6.

Table 6 - Optimal formulation for GEM loaded CH-PLGA NPs, determined by experimental design.

Parameter	Units	Optimal Value
PLGA mass	mg	13.9
PVA	%	3.61
EA Volume	µL	1998
Sonication cycles	#	6

In order to verify the protocol's efficacy, a formulation checkpoint was created in triplicate, implementing the optimal experimental values that were selected. Table 7 displays the predicted responses alongside the corresponding experimental results obtained during this validation process.

Table 7 - Model Validation (comparison between the predicted and experimental values). The results are represented as mean ± standard deviation (SD) (n=3).

		Size (nm)	Zeta Potential (mV)	PDI	EE (%)
Predicted	Mean	161	15.0	0.24	37.8
	Range	141 - 180	13.4 – 16.6	0.14 - 0.35	31.6 - 44.0
Experimental values		163 ± 14	22 ± 4	0.17 ± 0.02	33 ± 3

It can be seen from Table 7 that all the responses are in the range predicted by the software, except for the zeta potential. The zeta potential is slightly higher than predicted, which may be due to a greater solubilization of CH in the preparation of the NPs, and therefore a greater incorporation to the surface of the NP. Regarding the PDI, although it did not result in a significant analysis, the software correctly predicted its value. The prepared NPs present adequate physicochemical properties for their delivery to the brain, with sizes below 200 nm and PDI values below 0.2 (indicating a good homogeneity in NPs sizes). The positive zeta

potential allows their delivery to the brain by the intranasal route, as idealized. The EE value was maximized so that, keeping the specifications set for the answers, this is the maximum value possible to achieve. Although ideally it was intended that the EE had higher values, the value obtained is within the predicted range.

4.3 - Transmission electron microscopy

Analysis of the image obtained by TEM allows conclusions to be drawn about the shape and dimensions of the prepared NPs. In Figure 15 it is possible to observe the appearance of the produced GEM-loaded CH-PLGA NPs.

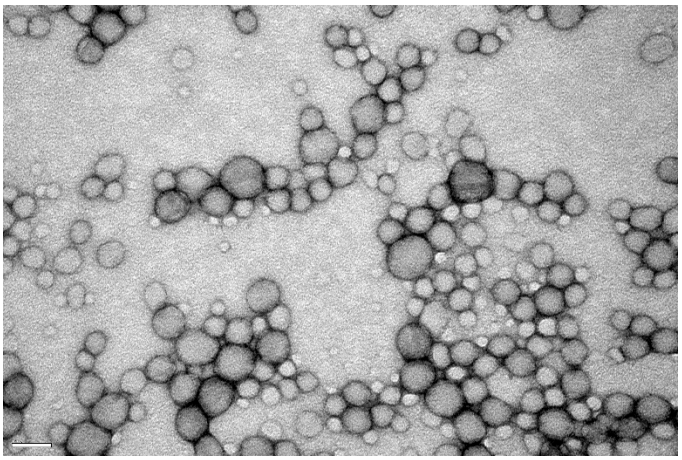

Figure 15 - TEM image of the prepared GEM loaded CH-PLGA NPs. Scale bar: 200 nm.

The depicted NPs have a regular and spherical shape, as expected [106]. The darker line that goes around the NPs corresponds to their coating, composed of PVA and CH. The sizes of the NPs analyzed by TEM are typically smaller than those obtained by DLS. This is due to the size measured by DLS being the hydrodynamic size of the NPs and not their actual size. This hydrodynamic size is related to variables such as particle interactions, polydispersion and hydration layers around the nanoparticles, which can lead to an overestimation of the size of the NPs measured in DLS measurements [107].

Additionally, it is possible to observe smaller and lighter spheres that correspond to PVA micelles. As in the preparation of the optimal NPs a PVA excess is used (3.61%), only a portion of the stabilizer is adsorbed at the NPs' surface, and rest remains forms micelles [108].

4.4 - FTIR analysis

FTIR analysis was used to confirm the successful modification of PLGA with CH, as well as the GEM incorporation in the developed NPs. Unloaded non-modified PLGA NPs were analyzed as control.

According to the literature, the FTIR spectrum of PLGA is composed of a prominent peak for C-O-C stretching seen at 1088 cm^{-1}, C-H stretching in methyl groups at 1460 cm^{-1}, a peak for C=O stretching at 1750 cm^{-1}, C-H stretching vibrations between 2850 and 3000 cm^{-1}, and O-H end group around 3500 cm^{-1} [109]. Regarding the FTIR absorbance spectrum of CH, stretching vibration of N-H and O-H groups is overlapped and linked to the specific band at 3414 cm^{-1} [110]. Strong peaks also occurred at 1545 cm^{-1} and 1630 cm^{-1} as a result of the amine and amide bonds in CH [111]. Through the analysis of Figure 16 it is possible to conclude that the results for control unloaded PLGA NPs and for CH polymer are in line with those mentioned in the literature.

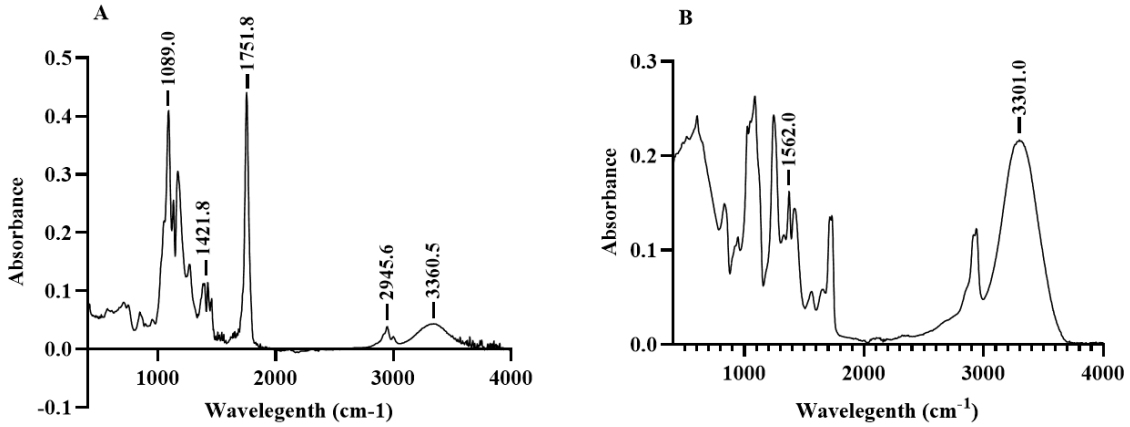

Figure 16 - FTIR absorbance spectrum of (A) unloaded PLGA NPs (B) CH solution for conjugation.

The FTIR analysis of the GEM-loaded PLGA NPs functionalized with CH is represented in the Figure 17 below, along with the spectrum of free GEM.

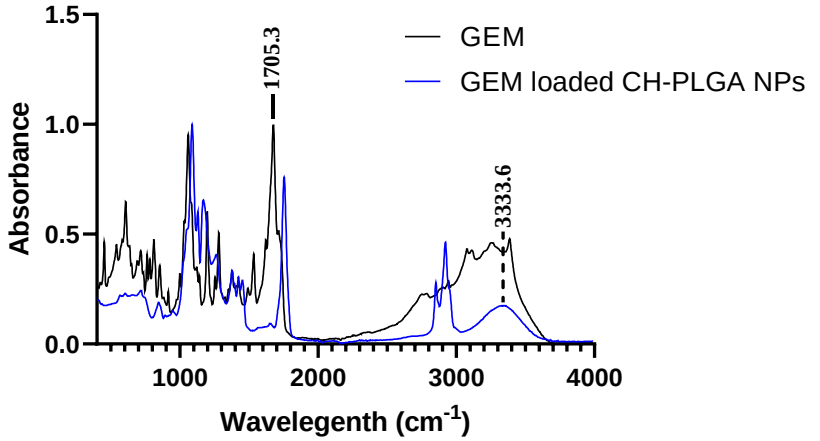

Figure 17 - FTIR absorbance spectrum of GEM and GEM loaded CH-PLGA.

The chitosan adsorption to the surface of PLGA NPs was proved by the greater presence of the characteristic band at 3200-3500 cm^{-1}, corresponding to the stretching vibration of NH_2 and OH groups [111].

According to the literature, the FTIR spectra of GEM displays amine bending vibrations at 1702 cm^{-1} and amine stretching vibrations at 3261 cm^{-1} [112]. Both GEM and GEM loaded CH-PLGA NPs are characterized by the presence of the band at 3333.6 cm^{-1} caused by O-H stretch as shown in Figure 17 [112]. A band at 1635 cm^{-1} in the GEM loaded CH-PLGA NPs, representing the bending of the NH group of GEM, would be expected to occur, which appears in the free GEM at about 1700 cm^{-1}, as mentioned [113]. The same does not occur and may be since a low amount of the incorporated GEM was adsorbed in the NPs' surface, being most of the drug entrapped in the polymeric matrix, and therefore not enough for its distinction from the spectrum of CH-PLGA NPs.

4.5 - GEM Release Profile

The GEM loaded CH-PLGA NPs were studied for the release of the encapsulated drug. In this way, the NPs were subjected to two different release conditions. The first, in which the NPs were suspended in PBS pH 7.4 and a second in which the NPs were suspended in PBS 6.4 containing 1 mg/mL lysozyme dissolved in the medium. The drug was determined to be soluble in its respective medium. Both release profiles were analyzed and are depicted in Figure 18.

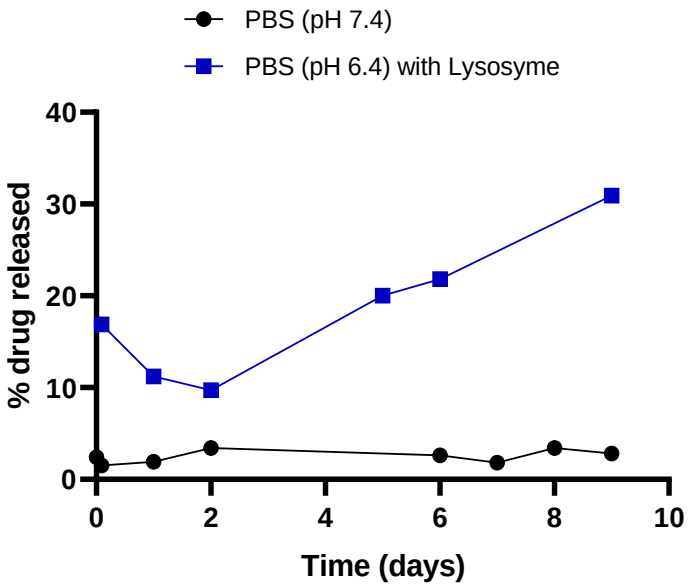

Figure 18 - *In vitro* release profile GEM loaded CH-PLGA NPs in PBS pH 7.4 (black line) and GEM loaded CH-PLGA NPs in PBS pH 6.4 with 1mg/mL of Lysozyme (blue line).

Drug release from PLGA NPs can occur by different mechanisms. Often, the portion of the drug adsorbed on the surface of the NPs is rapidly desorbed when the NPs are in contact with water, causing a rapid initial release [114]. In this case, no burst release of GEM was observed, which may suggest that the majority of the drug was trapped in the polymer matrix which is also in agreement with FTIR results.

The drug trapped in the polymeric matrix is released in a slower and more controlled manner, mainly through erosion, diffusion, and enzymatic degradation. Erosion is a release

mechanism that involves the degradation of ester bonds in the polymer chains. As hydrolysis of the ester bonds occurs, the structure of the PLGA weakens, allowing the encapsulated substance to be released gradually. The action of certain enzymes can catalyze the degradation of the polymer. This can be advantageous when the target site of the NPs has a significant concentration of a particular enzyme, and therefore promotes increased release at the desired site [114].

By studying both release profiles of GEM, it can be concluded that the release increased substantially in the presence of lysozyme. In fact, for the NPs suspended in PBS alone (pH 7.4), there is no significant drug release, not exceeding 3.5% after 9 days. This low release of the encapsulated drug suggested that something was preventing its exit. Possible causes could be the slow degradation of the CH layer, which prevents expulsion of PLGA chains to the water, preventing its degradation and subsequent release of the drug. To overcome this limitation, lysozyme was used to accelerate the degradation of the CH layer. NPs suspended in PBS (pH 6.4) with lysozyme showed a higher release profile, reaching 30.9% after 9 days. It was possible to denote significant changes in the size the NPs in presence of lysozyme as show in Figure 19, over the days of the drug release study.

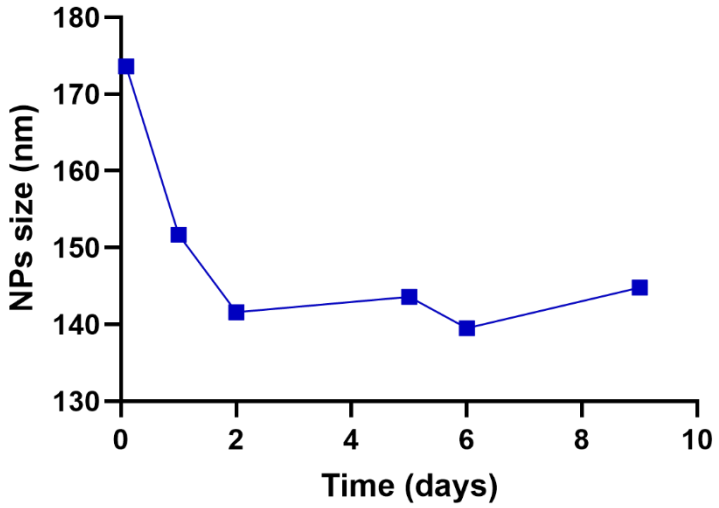

Figure 19 - Variation of size of NPs throughout the GEM release studies (PBS pH 6.4 with 1 mg/mL of Lysozyme).

Analyzing the previous Figure, it is possible to verify that the size of the NPs greatly varies from 174 nm to 152 after 2 days. This may be explained by acceleration of CH layer degradation by lysozyme, and therefore a decrease in the size of the NP.

The fact that GEM release is promoted by the action of this enzyme, which is overexpressed in the CSF of GBM patients, allows this release to be specific and triggered in the target tissue that is intended to be reached. In this way, it enables a higher concentration of GEM to be delivered to the target site.

4.6 - NPs stability in storage conditions

The properties of the NPs, including the mean size, PDI and zeta potential values, were measured on a weekly basis to assess the colloidal stability of the NPs over time. The stability of GEM-loaded CH-PLGA NPs suspended in ultrapure water (storage conditions) was analyzed for 10 weeks at 4 ºC, 4 weeks at 37 ºC and 6 weeks at room temperature. The results are summarized in tables 8, 9 and 10, respectively.

Table 8 - Mean size, PDI and zeta potential values for GEM loaded CH-PLGA NPs in storage conditions at 4 ºC (n=3). Data is presented as mean value ± SD.

	Stability at 4ºC		
	Size (nm)	**PDI**	**Zeta Potential (mV)**
week 0	163 ± 14	0.17 ± 0.02	24.0 ± 1.4
week 1	167 ± 17	0.21 ± 0.02	24.6 ± 1.8
week 2	165 ± 13	0.27 ± 0.03	24.2 ± 3.4
week 3	158 ± 9	0.17 ± 0.08	23.6 ± 4.0
week 4	152 ± 13	0.17 ± 0.07	22.5 ± 3.4
week 5	152 ± 15	0.17 ± 0.02	21.7 ± 1.4
week 6	155 ± 16	0.22 ± 0.03	20.6 ± 1.3
week 7	153 ± 15	0.20 ± 0.02	20.7 ± 2.0
week 8	146 ± 3	0.21 ± 0.02	17.7 ± 1.9
week 9	145 ± 4	0.20 ± 0.06	15.0 ± 3.8
week 10	145 ± 6	0.14 ± 0.04	17.6 ± 1.9

Table 9 - Mean size, PDI and zeta potential values for GEM loaded CH-PLGA NPs in storage conditions at 37°C (n=3). Data is presented as mean value ± SD.

	Stability at 37 ºC		
	Size (nm)	**PDI**	**Zeta Potential (mV)**
week 0	164 ± 1	0.27 ± 0.06	27.1 ± 1.4
week 1	160 ± 7	0.18 ± 0.06	13.5 ± 3.5
week 2	152 ± 7	0.20 ± 0.03	5.4 ± 1.1
week 3	145 ± 18	0.22 ± 0.05	5.5 ± 11.5
week 4	170 ± 8	0.24 ± 0.06	8.5 ± 16.5

Table 10 - Mean size, PDI and zeta potential values for GEM loaded CH-PLGA NPs in storage conditions at room temperature (n=3). Data is presented as mean value ± SD.

Stability at room temperature			
	Size (nm)	**PDI**	**Zeta Potential (mV)**
week 0	164 ± 1	0.27 ± 0.06	27.1 ± 1.4
week 1	145 ± 2	0.19 ± 0.03	7.7 ± 4.9
week 2	148 ± 1	0.17 ± 0.01	-0.3 ± 0.04
week 3	143 ± 21	0.22 ± 0.08	-4.7 ± 1.0
week 4	131 ±13	0.15 ± 0.04	-9.8 ± 2.1
week 5	155 ± 8	0.30 ± 0.04	-6.9 ± 0.7
week 6	157 ± 25	0.33 ± 0.15	-7.2 ± 0.7

The GEM-loaded CH-PLGA NPs proved to be stable over time under the three storage conditions studied, for size and PDI. This means that, no statistically significant changes were observed in these properties over the analyzed weeks ($p>0.05$). With regards to the zeta potential, it changed significantly over time ($p<0.05$). In fact, a decrease in zeta potential was observed, which can be justified by the degradation of the CH layer around the NP, leading the negative charge of the PLGA to be revealed. However, the zeta potential changes are much less prominent for the NPs stored at 4 ºC, suggesting a much slower rate of chitosan degradation. For this reason, 4 ºC is the most suitable condition to store the NPs.

4.7 - NPs stability in simulated physiological conditions

The average size, PDI and zeta potential values of the NPs were measured weekly to evaluate their colloidal stability under physiological conditions. The stability of GEM loaded CH-PLGA NPs in PBS was evaluated at three different pHs: pH 5.8 (to mimic nasal mucosa), pH 6.4 (to simulate tumor tissues) and pH 7.4 (to represent normal healthy tissues). The summarized results can be found in Tables 11, 12 and 13, respectively.

Table 11 - Mean size, PDI and zeta potential values for GEM loaded CH-PLGA NPs in physiological conditions at PBS pH 5.8 (n=3). Data is presented as mean value ± SD.

Stability at PBS pH 5.8			
	Size (nm)	**PDI**	**Zeta Potential (mV)**
week 0	151 ± 6	0.23 ± 0.08	-1.0 ± 0.3
week 1	116 ± 2	0.10 ± 0.02	-1.7 ± 0.6
week 2	110 ± 1	0.17 ± 0.07	-1.4 ± 0.7
week 3	112 ± 5	0.15 ± 0.04	-1.8 ± 0.1
week 4	117 ± 9	0.25 ± 0.02	-3.4 ± 1.1
week 5	116 ± 12	0.24 ± 0.01	-3.7 ± 0.9
week 6	115 ± 11	0.24 ± 0.02	-2.9 ± 0.6

Table 12 - Mean size, PDI and zeta potential values for GEM loaded CH-PLGA NPs in physiological conditions at PBS pH 6.4 (n=3). Data is presented as mean value ± SD.

Stability at PBS pH 6.4			
	Size (nm)	**PDI**	**Zeta Potential (mV)**
week 0	147 ± 3	0.22 ± 0.05	-1.8 ± 0.6
week 1	110 ± 2	0.08 ± 0.03	-3.3 ± 0.1
week 2	109 ± 2	0.10 ± 0.04	-2.5 ± 0.2
week 3	106 ± 2	0.13 ± 0.03	-3.3 ± 0.5
week 4	114 ± 3	0.29 ± 0.03	-3.8 ± 0.8
week 5	108 ± 3	0.25 ± 0.05	-3.6 ± 0.9
week 6	116 ± 5	0.23 ± 0.05	-3.2 ± 0.7

Table 13 - Mean size, PDI and zeta potential values for GEM loaded CH-PLGA NPs in physiological conditions at PBS pH 7.4 (n=3). Data is presented as mean value ± SD.

Stability at PBS pH 7.4			
	Size (nm)	**PDI**	**Zeta Potential (mV)**
week 0	147 ± 3	0.23 ± 0.05	-0.9 ± 0.2
week 1	118 ± 6	0.16 ± 0.06	-2.4 ± 1.0
week 2	123 ± 7	0.22 ± 0.07	-2.0 ± 0.4
week 3	112 ± 8	0.21 ± 0.03	-3.1 ± 1.7
week 4	118 ± 11	0.26 ± 0.04	-3.6 ± 1.1
week 5	117 ± 12	0.28 ± 0.07	-3.5 ± 1.4
week 6	110 ± 7	0.25 ± 0.05	-3.2 ± 1.0

The GEM-loaded CH-PLGA NPs showed stability over time under the three physiological conditions investigated, for PDI and zeta potential. Thus, it can be concluded that for NPs suspended in PBS of varying pH between 5.8 and 7.4, their physicochemical properties, such as PDI and zeta potential, did not change in a statistically significant way ($p>0.05$).

The NPs all exhibit charges close to zero and this is due to the effect of the PBS. The ability of the PBS to act as a buffer and neutralize the surface charges on the NPs can result in a zeta potential that is near zero when the particles are in suspension, since there is an interaction between the free charges present in the PBS and the chemical groups on the surface of the NPs [115]. Regarding size, a significant decrease in size is observed ($p<0.05$), for all physiological conditions analyzed. The decrease in size may be due to hydrolysis of the NPs from both the CH layer and the PLGA that allow the drug to be released. Regarding the stability in simulated nasal mucosa pH, since the NPs' will be retained for only a short period of time, the amount of drug release should not be relevant. In future work, the release will be studied in that conditions.

4.8 - NPs' Antiproliferative Activity

The antiproliferative activity of free GEM and GEM loaded CH-PLGA NPs was tested in two distinct human GBM cell lines (U251 and T98G). These lines have different expressions of the MGMT protein. The T98G cell line, due to its MGMT enzyme activity, shows greater resistance to alkylating agents, the main limitation of conventional therapy that this work intends to overcome. Figure 20 shows the survival inhibition curves for each cell line, for increasing concentrations of free GEM and GEM loaded CH-PLGA NPs.

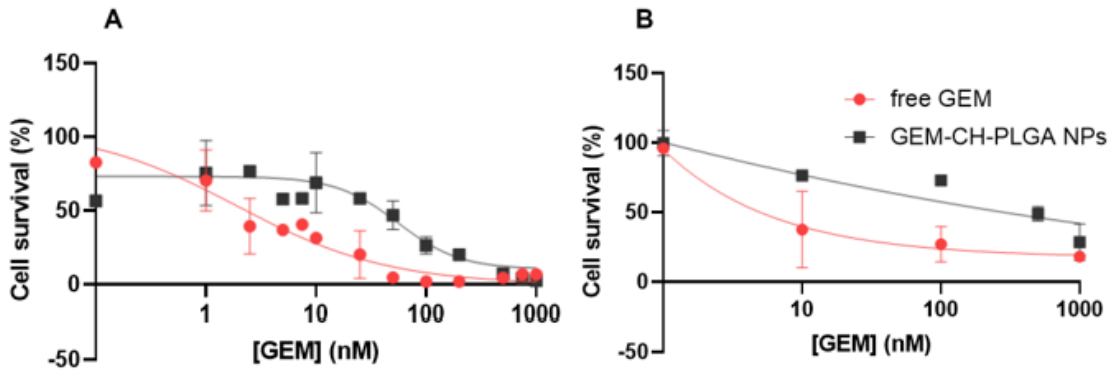

Figure 20 - Cell survival inhibition curve after 72h treatment with GEM and GEM loaded CH-PLGA NPs, on GBM human cells (A) U251 cell line and (B) T98G cell line. Cell survival is presented as percent [(%) = ((T)/(C)) x 100]. The results are represented as mean ± SD (n=3).

Both curves demonstrated that free GEM and GEM loaded CH-PLGA NPs induced a decrease in cell survival of both lines with increasing concentration. Thus, it was possible to calculate the IC_{50} value for each case, represented in Table 14. The IC_{50} represents, in this case, the GEM concentration required to inhibit 50 percent of cell survival. The lower the IC_{50} value, the greater the ability to inhibit cell proliferation [116].

Table 14 - Cytotoxic effects of U251 and T98G cell survival. Results are expressed as IC_{50} values at 72h exposure with free GEM and GEM loaded CH-PLGA NPS.

	IC_{50} (nM)	
	Free GEM	**GEM-CH-PLGA NPs**
U251	3.6 ± 2.7	34.8 ± 8.2
T98G	10.4 ± 12.2	351 ± 311

Analyzing the IC_{50} values results suggest that because GEM loaded CH-PLGA NPs have a higher IC_{50} value in both cell lines, they are less effective in inhibiting cell survival than free GEM. However, these results can be justified and related to the drug release study done earlier. The release results showed that after 72 h (period of incubation of the cells with the

treatment), only a small percentage of GEM was able to be released. Thus, the concentration of GEM placed in the NPs is not all available for cell treatment during that period of time.

The biocompatibility of CH-PLGA NPs on both cell lines was also tested, which is demonstrated in Figure 21.

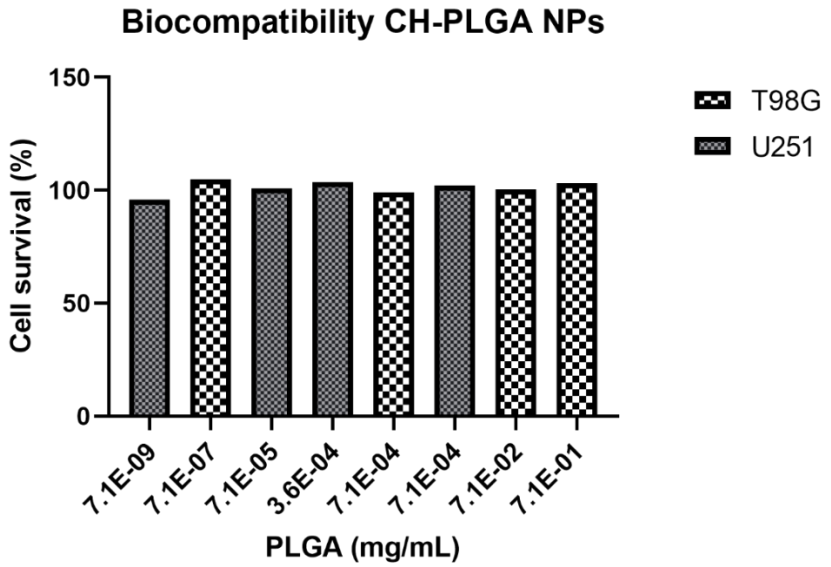

Figure 21 - Cell survival in both cell lines (U251 and T98G) after 72 h treatment with CH-PLGA NPs.

Analyzing the previous figure, it is possible to conclude that CH-PLGA NPs are biocompatible, since they show no toxicity in the tested concentration range. Thus, it is confirmed that the effect of inhibition of cell survival that was observed in GEM loaded CH-PLGA NPs is due entirely to the encapsulated drug. The concentration range of PLGA studied was chosen based on the range used of PLGA in the GEM loaded CH-PLGA NPs, employed in the cell tests.

Thus, GEM loaded CH-PLGA NPs proved to be able to cause inhibition of cell survival. Due to the slow and controlled release of the drug, this inhibition was shown to be less than that caused by free GEM in both cell lines, for an incubation period of 72 h. However, it is expected that the NPs are able to improve drug efficacy *in vivo*, by directing the drug to the target tissue, while free administered drug would distribute through the entire body.

Chapter 5

Conclusion and Future Perspectives

In recent decades, nanotechnology has become the basis of many applications, specifically in the medical field. Nanomedicine has thus emerged as a promising strategy for combating limitations that can be overcome with nano-sized particles. These particles have interesting characteristics and allow important improvements in the treatment and detection of cancers.

Thus, in this work it was proposed the use of NPs for GEM delivery for GBM therapy. NPs with sizes and zeta potentials suitable for intranasal administration have been produced. The experimental design proved to be very useful in optimizing the NPs. The developed model predicted effectively since the characteristics of the prepared NPs matched what was expected by the software. An optimized formulation was obtained, which has the following average properties: size = 163 ± 14 nm, PDI = 0.17 ± 0.02, zeta potential = 21.5 ± 3.9 mV and EE = 32.9 ± 3.1%.

The controlled release of GEM was studied, revealing a more significant release when the enzyme lysozyme, responsible for the degradation of the CH layer, was used. Thus, it can be concluded that the release of GEM occurs in a slow and controlled way, reaching 30.9% after 9 days. Furthermore, this mechanism allows for a release of the encapsulated drug in the desired tissue since lysozyme is overexpressed in the CSF of GBM patients. As the drug released is greater in the presence of this enzyme, a higher release will occur in the target tissue and therefore a higher concentration of GEM in the desired location.

The stability of the prepared NPs was examined under both storage and physiological conditions. When subjected to storage conditions, no significant alterations were observed in terms of NPs' size and PDI. However, a reduction in zeta potential was noted over time, potentially attributed to the degradation of the CH layer. On the other hand, under physiological conditions, the NPs displayed stability in terms of PDI and zeta potential. Although a decrease in size was observed, it is likely due to the hydrolysis of the NPs necessary for drug release.

The antiproliferative effect of the prepared NPs was studied in two human GBM cell lines (U251 and T98G). The tests performed on cells confirmed that CH-PLGA NPs with encapsulated GEM have the ability to inhibit cell survival. In addition, the biocompatibility of the CH-PLGA NPs was proven, as they showed no toxicity in the tested cells.

Additional experimental studies will be needed to evaluate the efficacy of the nanosystem. Future work may involve conducting drug release studies simulating the physiological conditions found in the nasal cavity (pH 5.8) and perform cellular studies in more GBM cell lines. Future *in vivo* trials using animal models could also be conducted, including pharmacokinetic and biodistribution studies, in order to deepen the understanding on the performance of the developed nanosystem.

References

[1] C. Alifieris and D. T. Trafalis, “Glioblastoma multiforme: Pathogenesis and treatment,” *Pharmacol. Ther.*, vol. 152, pp. 63–82, Jun. 2015, doi: 10.1016/J.PHARMTHERA.2015.05.005.

[2] S. K. Carlsson, S. P. Brothers, and C. Wahlestedt, “Emerging treatment strategies for glioblastoma multiforme,” *EMBO Mol. Med.*, vol. 6, no. 11, pp. 1359–1370, Nov. 2014, doi: 10.15252/EMMM.201302627.

[3] Y. Jia and J. Xie, “Promising molecular mechanisms responsible for gemcitabine resistance in cancer,” *Genes Dis.*, vol. 2, no. 4, pp. 299–306, Dec. 2015, doi: 10.1016/J.GENDIS.2015.07.003.

[4] C. Bastiancich, G. Bastiat, and F. Lagarce, “Gemcitabine and glioblastoma: challenges and current perspectives,” *Drug Discov. Today*, vol. 23, no. 2, pp. 416–423, Feb. 2018, doi: 10.1016/J.DRUDIS.2017.10.010.

[5] S. Ding *et al.*, “Overcoming blood–brain barrier transport: Advances in nanoparticle-based drug delivery strategies,” *Mater. Today*, vol. 37, pp. 112–125, Jul. 2020, doi: 10.1016/J.MATTOD.2020.02.001.

[6] J. Xie, Z. Shen, Y. Anraku, K. Kataoka, and X. Chen, “Nanomaterial-based blood-brain-barrier (BBB) crossing strategies,” *Biomaterials*, vol. 224, p. 119491, Dec. 2019, doi: 10.1016/J.BIOMATERIALS.2019.119491.

[7] M. C. Veronesi, M. Alhamami, S. B. Miedema, Y. Yun, M. Ruiz-Cardozo, and M. W. Vannier, “Imaging of intranasal drug delivery to the brain,” *Am. J. Nucl. Med. Mol. Imaging*, vol. 10, no. 1, p. 1, 2020.

[8] J. T. Duskey *et al.*, “Investigating Novel Syntheses of a Series of Unique Hybrid PLGA-Chitosan Polymers for Potential Therapeutic Delivery Applications,” *Polym. 2020, Vol. 12, Page 823*, vol. 12, no. 4, p. 823, Apr. 2020, doi: 10.3390/POLYM12040823.

[9] K. Urbanska, J. Sokolowska, M. Szmidt, and P. Sysa, “Glioblastoma multiforme – an overview,” *Contemp. Oncol. Onkol.*, vol. 18, no. 5, pp. 307–312, 2014, doi: 10.5114/WO.2014.40559.

[10] F. Pourgholi, M. hajivalili, J. N. Farhad, H. S. Kafil, and M. Yousefi, “Nanoparticles: Novel vehicles in treatment of Glioblastoma,” *Biomed. Pharmacother.*, vol. 77, pp. 98–107, Feb. 2016, doi: 10.1016/J.BIOPHA.2015.12.014.

[11] A. F. Tamimi and M. Juweid, “Epidemiology and Outcome of Glioblastoma,” *Exon Publ.*, pp. 143–153, Sep. 2017, doi: 10.15586/CODON.GLIOBLASTOMA.2017.CH8.

[12] D. Simińska *et al.*, “Epidemiology of Anthropometric Factors in Glioblastoma Multiforme—Literature Review,” *Brain Sci. 2021, Vol. 11, Page 116*, vol. 11, no. 1, p. 116, Jan. 2021, doi: 10.3390/BRAINSCI11010116.

[13] S. Grochans *et al.*, “Epidemiology of Glioblastoma Multiforme - Literature Review,” *Cancers 2022, Vol. 14, Page 2412*, vol. 14, no. 10, p. 2412, May 2022, doi: 10.3390/CANCERS14102412.

[14] A. C. Tan, D. M. Ashley, G. Y. López, M. Malinzak, H. S. Friedman, and M. Khasraw, “Management of glioblastoma: State of the art and future directions,” *CA. Cancer J. Clin.*, vol. 70, no. 4, pp. 299–312, Jul. 2020, doi: 10.3322/CAAC.21613.

[15] I. Crespo *et al.*, “Molecular and Genomic Alterations in Glioblastoma Multiforme,” *Am.*

J. Pathol., vol. 185, no. 7, pp. 1820–1833, Jul. 2015, doi: 10.1016/J.AJPATH.2015.02.023.

[16] C. R. Goodwin *et al.*, "Extraneural Glioblastoma Multiforme Vertebral Metastasis," *World Neurosurg.*, vol. 89, pp. 578-582.e3, May 2016, doi: 10.1016/J.WNEU.2015.11.061.

[17] M. Lemos Vieira Da Cunha, M. Vinicius, C. Maldaun, M. Lemos, and V. Da Cunha, "Metastasis from glioblastoma multiforme: a meta-analysis," *Rev. Assoc. Med. Bras.*, vol. 65, no. 3, pp. 424–433, Mar. 2019, doi: 10.1590/1806-9282.65.3.424.

[18] F. Hanif, K. Muzaffar, K. Perveen, S. M. Malhi, and S. U. Simjee, "Glioblastoma Multiforme: A Review of its Epidemiology and Pathogenesis through Clinical Presentation and Treatment," *Asian Pac. J. Cancer Prev.*, vol. 18, no. 1, p. 3, 2017, doi: 10.22034/APJCP.2017.18.1.3.

[19] S. Rasheed, K. Rehman, and M. S. H. Akash, "An insight into the risk factors of brain tumors and their therapeutic interventions," *Biomed. Pharmacother.*, vol. 143, p. 112119, Nov. 2021, doi: 10.1016/J.BIOPHA.2021.112119.

[20] M. E. Davis, "Glioblastoma: Overview of Disease and Treatment," *Clin. J. Oncol. Nurs.*, vol. 20, no. 5, p. S2, Oct. 2016, doi: 10.1188/16.CJON.S1.2-8.

[21] M. J. Ramalho *et al.*, "Receptor-mediated PLGA nanoparticles for glioblastoma multiforme treatment," *Int. J. Pharm.*, vol. 545, no. 1–2, pp. 84–92, Jul. 2018, doi: 10.1016/J.IJPHARM.2018.04.062.

[22] M. J. Ramalho, S. Andrade, M. Á. N. Coelho, J. A. Loureiro, and M. C. Pereira, "Biophysical interaction of temozolomide and its active metabolite with biomembrane models: The relevance of drug-membrane interaction for Glioblastoma Multiforme therapy," *Eur. J. Pharm. Biopharm.*, vol. 136, pp. 156–163, Mar. 2019, doi: 10.1016/J.EJPB.2019.01.015.

[23] R. Della Monica *et al.*, "MGMT and Whole-Genome DNA Methylation Impacts on Diagnosis, Prognosis and Therapy of Glioblastoma Multiforme," *Int. J. Mol. Sci. 2022, Vol. 23, Page 7148*, vol. 23, no. 13, p. 7148, Jun. 2022, doi: 10.3390/IJMS23137148.

[24] N. Senhaji, A. S. Houssaini, S. Lamrabet, S. Louati, and S. Bennis, "Molecular and Circulating Biomarkers in Patients with Glioblastoma," *Int. J. Mol. Sci. 2022, Vol. 23, Page 7474*, vol. 23, no. 13, p. 7474, Jul. 2022, doi: 10.3390/IJMS23137474.

[25] M. Schneider *et al.*, "Inhibition of Intercellular Cytosolic Traffic via Gap Junctions Reinforces Lomustine-Induced Toxicity in Glioblastoma Independent of MGMT Promoter Methylation Status," *Pharm. 2021, Vol. 14, Page 195*, vol. 14, no. 3, p. 195, Feb. 2021, doi: 10.3390/PH14030195.

[26] K. Seystahl, W. Wick, and M. Weller, "Therapeutic options in recurrent glioblastoma—An update," *Crit. Rev. Oncol. Hematol.*, vol. 99, pp. 389–408, Mar. 2016, doi: 10.1016/J.CRITREVONC.2016.01.018.

[27] S. Alomari *et al.*, "Drug Repurposing for Glioblastoma and Current Advances in Drug Delivery-A Comprehensive Review of the Literature," *Biomol. 2021, Vol. 11, Page 1870*, vol. 11, no. 12, p. 1870, Dec. 2021, doi: 10.3390/BIOM11121870.

[28] J. Basso, A. Miranda, J. Sousa, A. Pais, and C. Vitorino, "Repurposing drugs for glioblastoma: From bench to bedside," *Cancer Lett.*, vol. 428, pp. 173–183, Aug. 2018, doi: 10.1016/J.CANLET.2018.04.039.

[29] S. Masoumi *et al.*, "Understanding cytoskeleton regulators in glioblastoma multiforme for therapy design," *Drug Des. Devel. Ther.*, vol. 10, p. 2881, Sep. 2016, doi: 10.2147/DDDT.S106196.

[30] L. Guarnaccia *et al.*, "Frontiers in Anti-Cancer Drug Discovery: Challenges and Perspectives of Metformin as Anti-Angiogenic Add-On Therapy in Glioblastoma," *Cancers 2022, Vol. 14, Page 112*, vol. 14, no. 1, p. 112, Dec. 2021, doi: 10.3390/CANCERS14010112.

[31] C. Seliger *et al.*, "Use of metformin and outcome of patients with newly diagnosed glioblastoma: Pooled analysis," *Int. J. Cancer*, vol. 146, no. 3, pp. 803–809, Feb. 2020, doi: 10.1002/IJC.32337.

[32] G. Shenouda *et al.*, "A Phase 2 Study of Neo-adjuvant Metformin and Temozolomide followed by Hypofractionated Accelerated RadioTherapy (HART) with Concomitant and Adjuvant Metformin and Temozolomide (TMZ) in Patients with Glioblastoma," *Int. J. Radiat. Oncol.*, vol. 108, no. 3, p. S21, Nov. 2020, doi: 10.1016/j.ijrobp.2020.07.2107.

[33] C. Happold *et al.*, “Does Valproic Acid or Levetiracetam Improve Survival in Glioblastoma? A Pooled Analysis of Prospective Clinical Trials in Newly Diagnosed Glioblastoma,” *J. Clin. Oncol.*, vol. 34, no. 7, p. 731, Mar. 2016, doi: 10.1200/JCO.2015.63.6563.

[34] A. V. Krauze *et al.*, “A Phase 2 Study of Concurrent Radiation Therapy, Temozolomide, and the Histone Deacetylase Inhibitor Valproic Acid for Patients With Glioblastoma,” *Int. J. Radiat. Oncol.*, vol. 92, no. 5, pp. 986–992, Aug. 2015, doi: 10.1016/J.IJROBP.2015.04.038.

[35] S. Maraka *et al.*, “Phase 1 lead-in to a phase 2 factorial study of temozolomide plus memantine, mefloquine, and metformin as postradiation adjuvant therapy for newly diagnosed glioblastoma,” *Cancer*, vol. 125, no. 3, pp. 424–433, Feb. 2019, doi: 10.1002/CNCR.31811.

[36] S. Yang, D. Luo, N. Li, C. Li, S. Tang, and Z. Huang, “New Mechanism of Gemcitabine and Its Phosphates: DNA Polymerization Disruption via 3′-5′ Exonuclease Inhibition,” *Biochemistry*, vol. 59, no. 45, pp. 4344–4352, Nov. 2020, doi: https://doi.org/10.1021/acs.biochem.0c00543.

[37] A. Ferreira, R. Lapa, and N. Vale, “Combination of Gemcitabine with Cell-Penetrating Peptides: A Pharmacokinetic Approach Using in Silico Tools,” *Biomol. 2019, Vol. 9, Page 693*, vol. 9, no. 11, p. 693, Nov. 2019, doi: 10.3390/BIOM9110693.

[38] P. Y. Liyanage *et al.*, “Pediatric glioblastoma target-specific efficient delivery of gemcitabine across the blood–brain barrier via carbon nitride dots,” *Nanoscale*, vol. 12, no. 14, pp. 7927–7938, Apr. 2020, doi: 10.1039/D0NR01647K.

[39] G. Carpinelli *et al.*, “Gemcitabine Treatment of Experimental C6 Glioma: The Effects on Cell Cycle and Apoptotic Rate,” *Anticancer Res.*, vol. 26, no. 4B, pp. 3017–3024, Jul. 2006, Accessed: Dec. 22, 2022.

[40] M. El-Naggar, M. Omar, A. Elgeriany, G. J. Peters, A. Mostafa, and S. Shehata, “Gemcitabine followed by radiotherapy in treatment of newly diagnosed high-grade gliomas,” *J. Cancer Metastasis Treat.*, vol. 2, no. 5, pp. 188–194, May 2016, doi: 10.20517/2394-4722.2016.15.

[41] S. E. M. Veldhuijzen van Zanten *et al.*, “A phase I/II study of gemcitabine during radiotherapy in children with newly diagnosed diffuse intrinsic pontine glioma,” *J. Neurooncol.*, vol. 135, no. 2, pp. 307–315, Nov. 2017, doi: 10.1007/S11060-017-2575-9/TABLES/2.

[42] L. Leon, E. J. Chung, and C. Rinaldi, “A brief history of nanotechnology and introduction to nanoparticles for biomedical applications,” *Nanoparticles Biomed. Appl. Fundam. Concepts, Biol. Interact. Clin. Appl.*, pp. 1–4, Jan. 2020, doi: 10.1016/B978-0-12-816662-8.00001-1.

[43] M. Zain *et al.*, “Applications of nanotechnology in biological systems and medicine,” *Nanotechnol. Hematol. Blood Transfusion, Artif. Blood*, pp. 215–235, Jan. 2022, doi: 10.1016/B978-0-12-823971-1.00019-2.

[44] A. K. Pearce and R. K. O’Reilly, “Insights into Active Targeting of Nanoparticles in Drug Delivery: Advances in Clinical Studies and Design Considerations for Cancer Nanomedicine,” *Bioconjug. Chem.*, vol. 30, no. 9, pp. 2300–2311, Sep. 2019, doi: 10.1021/ACS.BIOCONJCHEM.9B00456/ASSET/IMAGES/LARGE/BC9B00456_0007.JPEG.

[45] E. Garbayo, S. Pascual-Gil, C. Rodríguez-Nogales, L. Saludas, A. Estella-Hermoso de Mendoza, and M. J. Blanco-Prieto, “Nanomedicine and drug delivery systems in cancer and regenerative medicine,” *Wiley Interdiscip. Rev. Nanomedicine Nanobiotechnology*, vol. 12, no. 5, p. e1637, Sep. 2020, doi: 10.1002/WNAN.1637.

[46] S. A. A. Rizvi and A. M. Saleh, “Applications of nanoparticle systems in drug delivery technology,” *Saudi Pharm. J. SPJ*, vol. 26, no. 1, p. 64, Jan. 2018, doi: 10.1016/J.JSPS.2017.10.012.

[47] Y. Yao *et al.*, “Nanoparticle-Based Drug Delivery in Cancer Therapy and Its Role in Overcoming Drug Resistance,” *Front. Mol. Biosci.*, vol. 7, p. 193, Aug. 2020, doi: 10.3389/FMOLB.2020.00193/BIBTEX.

[48] M. J. Mitchell, M. M. Billingsley, R. M. Haley, M. E. Wechsler, N. A. Peppas, and R. Langer, “Engineering precision nanoparticles for drug delivery,” *Nat. Rev. Drug Discov. 2020 202*, vol. 20, no. 2, pp. 101–124, Dec. 2020, doi: 10.1038/s41573-020-0090-8.

[49] R. Pandit, L. Chen, and J. Götz, “The blood-brain barrier: Physiology and strategies for

drug delivery," *Adv. Drug Deliv. Rev.*, vol. 165–166, pp. 1–14, Jan. 2020, doi: 10.1016/J.ADDR.2019.11.009.

[50] E. G. Knox, M. R. Aburto, G. Clarke, J. F. Cryan, and C. M. O'Driscoll, "The blood-brain barrier in aging and neurodegeneration," *Mol. Psychiatry 2022 276*, vol. 27, no. 6, pp. 2659–2673, Mar. 2022, doi: 10.1038/s41380-022-01511-z.

[51] M. J. Ramalho, J. A. Loureiro, M. A. N. Coelho, and M. C. Pereira, "Transferrin Receptor-Targeted Nanocarriers: Overcoming Barriers to Treat Glioblastoma," *Pharm. 2022, Vol. 14, Page 279*, vol. 14, no. 2, p. 279, Jan. 2022, doi: 10.3390/PHARMACEUTICS14020279.

[52] J. J. Mulvihill, E. M. Cunnane, A. M. Ross, J. T. Duskey, G. Tosi, and A. M. Grabrucker, "Drug delivery across the blood–brain barrier: recent advances in the use of nanocarriers," vol. 15, no. 2, pp. 205–214, Jan. 2020, doi: 10.2217/NNM-2019-0367.

[53] D. S. Hersh *et al.*, "Evolving Drug Delivery Strategies to Overcome the Blood Brain Barrier," *Curr. Pharm. Des.*, vol. 22, no. 9, pp. 1177–1193, Mar. 2016, doi: 10.2174/1381612822666151221150733.

[54] M. M. Patel and B. M. Patel, "Crossing the Blood-Brain Barrier: Recent Advances in Drug Delivery to the Brain," *CNS Drugs*, vol. 31, no. 2, pp. 109–133, Feb. 2017, doi: 10.1007/S40263-016-0405-9.

[55] M. J. Fowler, J. D. Cotter, B. E. Knight, E. M. Sevick-Muraca, D. I. Sandberg, and R. W. Sirianni, "Intrathecal drug delivery in the era of nanomedicine," *Adv. Drug Deliv. Rev.*, vol. 165–166, pp. 77–95, Jan. 2020, doi: 10.1016/J.ADDR.2020.02.006.

[56] G. D. Cha *et al.*, "Advances in drug delivery technology for the treatment of glioblastoma multiforme," *J. Control. Release*, vol. 328, pp. 350–367, Dec. 2020, doi: 10.1016/J.JCONREL.2020.09.002.

[57] M. Westphal, Z. Ram, V. Riddle, D. Hilt, and E. Bortey, "Gliadel® wafer in initial surgery for malignant glioma: Long-term follow-up of a multicenter controlled trial," *Acta Neurochir. (Wien).*, vol. 148, no. 3, pp. 269–275, Feb. 2006, doi: 10.1007/S00701-005-0707-Z/METRICS.

[58] A. C. Correia, A. R. Monteiro, R. Silva, J. N. Moreira, J. M. Sousa Lobo, and A. C. Silva, "Lipid nanoparticles strategies to modify pharmacokinetics of central nervous system targeting drugs: Crossing or circumventing the blood-brain barrier (BBB) to manage neurological disorders," *Adv. Drug Deliv. Rev.*, vol. 189, Oct. 2022, doi: 10.1016/J.ADDR.2022.114485.

[59] S. Gänger and K. Schindowski, "Tailoring Formulations for Intranasal Nose-to-Brain Delivery: A Review on Architecture, Physico-Chemical Characteristics and Mucociliary Clearance of the Nasal Olfactory Mucosa," *Pharmaceutics*, vol. 10, no. 3, Sep. 2018, doi: 10.3390/PHARMACEUTICS10030116.

[60] N. N. Ferreira *et al.*, "Nose-to-brain co-delivery of drugs for glioblastoma treatment using nanostructured system," *Int. J. Pharm.*, vol. 603, p. 120714, Jun. 2021, doi: 10.1016/J.IJPHARM.2021.120714.

[61] D. H. Shin, S. Xuan, W. Y. Kim, G. U. Bae, and J. S. Kim, "CD133 antibody-conjugated immunoliposomes encapsulating gemcitabine for targeting glioblastoma stem cells," *J. Mater. Chem. B*, vol. 2, no. 24, pp. 3771–3781, May 2014, doi: 10.1039/C4TB00185K.

[62] C. Bastiancich *et al.*, "Evaluation of lauroyl-gemcitabine-loaded hydrogel efficacy in glioblastoma rat models," vol. 13, no. 16, pp. 1999–2013, Sep. 2018, doi: 10.2217/NNM-2018-0057.

[63] C. Bastiancich *et al.*, "Injectable nanomedicine hydrogel for local chemotherapy of glioblastoma after surgical resection," *J. Control. Release*, vol. 264, pp. 45–54, Oct. 2017, doi: 10.1016/J.JCONREL.2017.08.019.

[64] C. X. Wang *et al.*, "Antitumor effects of polysorbate-80 coated gemcitabine polybutylcyanoacrylate nanoparticles in vitro and its pharmacodynamics in vivo on C6 glioma cells of a brain tumor model," *Brain Res.*, vol. 1261, pp. 91–99, Mar. 2009, doi: 10.1016/J.BRAINRES.2009.01.011.

[65] F. Sahli, M. Courcelle, T. Palama, N. Djaker, P. Savarin, and J. Spadavecchia, "Temozolomide, Gemcitabine, and Decitabine Hybrid Nanoconjugates: From Design to Proof-of-Concept (PoC) of Synergies toward the Understanding of Drug Impact on Human Glioblastoma Cells," *J. Med. Chem.*, vol. 63, no. 13, pp. 7410–7421, Jul. 2020, doi: 10.1021/ACS.JMEDCHEM.0C00694.

[66] Q. Mu, G. Lin, V. K. Patton, K. Wang, O. W. Press, and M. Zhang, "Gemcitabine and

chlorotoxin conjugated iron oxide nanoparticles for glioblastoma therapy," *J. Mater. Chem. B*, vol. 4, no. 1, pp. 32–36, Dec. 2015, doi: 10.1039/C5TB02123E.

[67] A. Gaudin *et al.*, "PEGylated squalenoyl-gemcitabine nanoparticles for the treatment of glioblastoma," *Biomaterials*, vol. 105, pp. 136–144, Oct. 2016, doi: 10.1016/J.BIOMATERIALS.2016.07.037.

[68] S. I. Ahmed *et al.*, "CD133 Expression in Glioblastoma Multiforme: A Literature Review," *Cureus*, vol. 10, no. 10, Oct. 2018, doi: 10.7759/CUREUS.3439.

[69] H.-J. Liu and P. Xu, "Strategies to overcome/penetrate the BBB for systemic nanoparticle delivery to the brain/brain tumor," *Adv. Drug Deliv. Rev.*, vol. 191, p. 114619, Dec. 2022, doi: 10.1016/J.ADDR.2022.114619.

[70] I. M. Fukuda, C. F. F. Pinto, C. D. S. Moreira, A. M. Saviano, and F. R. Lourenço, "Design of Experiments (DoE) applied to Pharmaceutical and Analytical Quality by Design (QbD)," *Brazilian J. Pharm. Sci.*, vol. 54, no. Special Issue, p. e01006, Nov. 2018, doi: 10.1590/S2175-97902018000001006.

[71] S. Bhattacharya and S. Bhattacharya, "Central Composite Design for Response Surface Methodology and Its Application in Pharmacy," *Response Surf. Methodol. Eng. Sci.*, Jan. 2021, doi: 10.5772/INTECHOPEN.95835.

[72] A. L. H. Müller, J. A. De Oliveira, O. D. Prestes, M. B. Adaime, and R. Zanella, "Design of experiments and method development," *Solid-Phase Extr.*, pp. 589–608, Jan. 2019, doi: 10.1016/B978-0-12-816906-3.00022-4.

[73] F. Babick, "Dynamic light scattering (DLS)," *Charact. Nanoparticles Meas. Process. Nanoparticles*, pp. 137–172, Jan. 2020, doi: 10.1016/B978-0-12-814182-3.00010-9.

[74] S. Falke and C. Betzel, "Dynamic Light Scattering (DLS)," in *Radiation in Bioanalysis*, Springer, Cham, 2019, pp. 173–193.

[75] K. Kaneko *et al.*, "Evaluation of polymer choice on immunogenicity of chitosan coated PLGA NPs with surface-adsorbed pneumococcal protein antigen PspA4Pro," *Int. J. Pharm.*, vol. 599, p. 120407, Apr. 2021, doi: 10.1016/J.IJPHARM.2021.120407.

[76] S. Bhattacharjee, "DLS and zeta potential – What they are and what they are not?," *J. Control. Release*, vol. 235, pp. 337–351, Aug. 2016, doi: 10.1016/J.JCONREL.2016.06.017.

[77] M. C. Smith, R. M. Crist, J. D. Clogston, and S. E. McNeil, "Zeta potential: a case study of cationic, anionic, and neutral liposomes," *Anal. Bioanal. Chem.*, vol. 409, no. 24, pp. 5779–5787, Sep. 2017, doi: 10.1007/S00216-017-0527-Z/FIGURES/4.

[78] W. Mäntele and E. Deniz, "UV–VIS absorption spectroscopy: Lambert-Beer reloaded," *Spectrochim. Acta Part A Mol. Biomol. Spectrosc.*, vol. 173, pp. 965–968, Feb. 2017, doi: 10.1016/J.SAA.2016.09.037.

[79] Â. Novais, A. R. Freitas, C. Rodrigues, and L. Peixe, "Fourier transform infrared spectroscopy: unlocking fundamentals and prospects for bacterial strain typing," *Eur. J. Clin. Microbiol. Infect. Dis. 2018 383*, vol. 38, no. 3, pp. 427–448, Nov. 2018, doi: 10.1007/S10096-018-3431-3.

[80] D. Titus, E. James Jebaseelan Samuel, and S. M. Roopan, "Nanoparticle characterization techniques," *Green Synth. Charact. Appl. Nanoparticles*, pp. 303–319, Jan. 2019, doi: 10.1016/B978-0-08-102579-6.00012-5.

[81] K. Y. Su and W. L. Lee, "Fourier Transform Infrared Spectroscopy as a Cancer Screening and Diagnostic Tool: A Review and Prospects," *Cancers 2020, Vol. 12, Page 115*, vol. 12, no. 1, p. 115, Jan. 2020, doi: 10.3390/CANCERS12010115.

[82] M. Malatesta, "Transmission Electron Microscopy as a Powerful Tool to Investigate the Interaction of Nanoparticles with Subcellular Structures," *Int. J. Mol. Sci. 2021, Vol. 22, Page 12789*, vol. 22, no. 23, p. 12789, Nov. 2021, doi: 10.3390/IJMS222312789.

[83] N. Braidy, A. Béchu, J. C. de Souza Terra, and G. S. Patience, "Experimental methods in chemical engineering: Transmission electron microscopy—TEM," *Can. J. Chem. Eng.*, vol. 98, no. 3, pp. 628–641, Mar. 2020, doi: 10.1002/CJCE.23692.

[84] C. Y. Tang and Z. Yang, "Transmission Electron Microscopy (TEM)," *Membr. Charact.*, pp. 145–159, Jan. 2017, doi: 10.1016/B978-0-444-63776-5.00008-5.

[85] A. Moscardini *et al.*, "Uranium-free X solution: a new generation contrast agent for biological samples ultrastructure," *Sci. Reports 2020 101*, vol. 10, no. 1, pp. 1–11, Jul. 2020, doi: 10.1038/s41598-020-68405-4.

[86] N. Mei, J. Hedberg, I. Odnevall Wallinder, and E. Blomberg, "Influence of Biocorona

Formation on the Transformation and Dissolution of Cobalt Nanoparticles under Physiological Conditions," *ACS Omega*, vol. 4, no. 26, pp. 21778–21791, Dec. 2019, doi: 10.1021/ACSOMEGA.9B02641/ASSET/IMAGES/LARGE/AO9B02641_0003.JPEG.

[87] Y. Wu, K. Wei, G. Ma, C. Ji, and M. Yin, "A heptamethine cyanine with meso-N-induced rearrangement for acid-activated tumour imaging and photothermal therapy," *Biomater. Sci.*, vol. 10, no. 11, pp. 2964–2971, May 2022, doi: 10.1039/D2BM00413E.

[88] G. Melinte, G. Selvolini, C. Cristea, and G. Marrazza, "Aptasensors for lysozyme detection: Recent advances," *Talanta*, vol. 226, p. 122169, May 2021, doi: 10.1016/J.TALANTA.2021.122169.

[89] N. Islam, I. Dmour, and M. O. Taha, "Degradability of chitosan micro/nanoparticles for pulmonary drug delivery," *Heliyon*, vol. 5, no. 5, p. e01684, May 2019, doi: 10.1016/J.HELIYON.2019.E01684.

[90] L. R. Michels *et al.*, "Nasal administration of a temozolomide-loaded thermoresponsive nanoemulsion reduces tumor growth in a preclinical glioblastoma model," *J. Control. Release*, vol. 355, pp. 343–357, Mar. 2023, doi: 10.1016/J.JCONREL.2023.01.070.

[91] J.-H. Tang *et al.*, "Bortezomib inhibits growth and sensitizes glioma to temozolomide (TMZ) via down-regulating the FOXM1–Survivin axis," *Cancer Commun.*, vol. 39, no. 1, p. 81, 2019, doi: 10.1186/s40880-019-0424-2.

[92] P. J. Vlachostergios, E. Hatzidaki, C. D. Befani, P. Liakos, and C. N. Papandreou, "Bortezomib overcomes MGMT-related resistance of glioblastoma cell lines to temozolomide in a schedule-dependent manner," *Invest. New Drugs*, vol. 31, no. 5, pp. 1169–1181, 2013, doi: 10.1007/s10637-013-9968-1.

[93] V. Vichai and K. Kirtikara, "Sulforhodamine B colorimetric assay for cytotoxicity screening," *Nat. Protoc.*, vol. 1, no. 3, pp. 1112–1116, 2006, doi: 10.1038/nprot.2006.179.

[94] N. P. Truong, M. R. Whittaker, C. W. Mak, and T. P. Davis, "The importance of nanoparticle shape in cancer drug delivery," *Expert Opin. Drug Deliv.*, vol. 12, no. 1, pp. 129–142, 2015, doi: 10.1517/17425247.2014.950564.

[95] Y.-H. Tsou *et al.*, "Drug Delivery to the Brain across the Blood–Brain Barrier Using Nanomaterials," *Small*, vol. 13, no. 43, p. 1701921, Nov. 2017, doi: 10.1002/SMLL.201701921.

[96] M. F. Attia, N. Anton, J. Wallyn, Z. Omran, and T. F. Vandamme, "An overview of active and passive targeting strategies to improve the nanocarriers efficiency to tumour sites," *J. Pharm. Pharmacol.*, vol. 71, no. 8, pp. 1185–1198, Jul. 2019, doi: 10.1111/JPHP.13098.

[97] M. J. Ramalho, J. A. Loureiro, M. A. N. Coelho, and M. C. Pereira, "Factorial Design as a Tool for the Optimization of PLGA Nanoparticles for the Co-Delivery of Temozolomide and O6-Benzylguanine," *Pharmaceutics*, vol. 11, no. 8, p. 401, Aug. 2019, doi: 10.3390/pharmaceutics11080401.

[98] Y. Liu, J. Pan, and S. S. Feng, "Nanoparticles of lipid monolayer shell and biodegradable polymer core for controlled release of paclitaxel: effects of surfactants on particles size, characteristics and in vitro performance," *Int. J. Pharm.*, vol. 395, no. 1–2, pp. 243–250, Aug. 2010, doi: 10.1016/J.IJPHARM.2010.05.008.

[99] E. Ruiz, V. H. Orozco, L. M. Hoyos, and L. F. Giraldo, "Study of sonication parameters on PLA nanoparticles preparation by simple emulsion-evaporation solvent technique," *Eur. Polym. J.*, vol. 173, p. 111307, Jun. 2022, doi: 10.1016/J.EURPOLYMJ.2022.111307.

[100] H. M. Aldawsari, N. A. Alhakamy, R. Padder, M. Husain, and S. Md, "Preparation and Characterization of Chitosan Coated PLGA Nanoparticles of Resveratrol: Improved Stability, Antioxidant and Apoptotic Activities in H1299 Lung Cancer Cells," *Coatings 2020, Vol. 10, Page 439*, vol. 10, no. 5, p. 439, Apr. 2020, doi: 10.3390/COATINGS10050439.

[101] S. Liu, S. Yang, and P. C. Ho, "Intranasal administration of carbamazepine-loaded carboxymethyl chitosan nanoparticles for drug delivery to the brain," *Asian J. Pharm. Sci.*, vol. 13, no. 1, pp. 72–81, Jan. 2018, doi: 10.1016/J.AJPS.2017.09.001.

[102] S. Chakraborty and P. K. Panigrahi, "Stability of nanofluid: A review," *Appl. Therm. Eng.*, vol. 174, p. 115259, Jun. 2020, doi: 10.1016/J.APPLTHERMALENG.2020.115259.

[103] M. V. Shaikh, M. Kala, and M. Nivsarkar, "Formulation and optimization of doxorubicin loaded polymeric nanoparticles using Box-Behnken design: ex-vivo stability and in-vitro

activity," *Eur. J. Pharm. Sci.*, vol. 100, pp. 262–272, Mar. 2017, doi: 10.1016/J.EJPS.2017.01.026.

[104] R. Saadati and S. Dadashzadeh, "Marked effects of combined TPGS and PVA emulsifiers in the fabrication of etoposide-loaded PLGA-PEG nanoparticles: In vitro and in vivo evaluation," *Int. J. Pharm.*, vol. 464, no. 1–2, pp. 135–144, Apr. 2014, doi: 10.1016/J.IJPHARM.2014.01.014.

[105] J. Varshosaz, S. Taymouri, H. Hamishehkar, R. Vatankhah, and S. Yaghubi, "Development of dry powder inhaler containing tadalafil-loaded PLGA nanoparticles," *Res. Pharm. Sci.*, vol. 12, no. 3, p. 222, Jun. 2017, doi: 10.4103/1735-5362.207203.

[106] L. Devi, R. Gupta, S. K. Jain, S. Singh, and P. Kesharwani, "Synthesis, characterization and in vitro assessment of colloidal gold nanoparticles of Gemcitabine with natural polysaccharides for treatment of breast cancer," *J. Drug Deliv. Sci. Technol.*, vol. 56, p. 101565, Apr. 2020, doi: 10.1016/J.JDDST.2020.101565.

[107] B. K. Wilson and R. K. Prud'homme, "Nanoparticle size distribution quantification from transmission electron microscopy (TEM) of ruthenium tetroxide stained polymeric nanoparticles," *J. Colloid Interface Sci.*, vol. 604, pp. 208–220, Dec. 2021, doi: 10.1016/J.JCIS.2021.04.081.

[108] H. Y. Kwon, J. Y. Lee, S. W. Choi, Y. Jang, and J. H. Kim, "Preparation of PLGA nanoparticles containing estrogen by emulsification–diffusion method," *Colloids Surfaces A Physicochem. Eng. Asp.*, vol. 182, no. 1–3, pp. 123–130, Jun. 2001, doi: 10.1016/S0927-7757(00)00825-6.

[109] Y. Wang, P. Li, and L. Kong, "Chitosan-modified PLGA nanoparticles with versatile surface for improved drug delivery," *AAPS PharmSciTech*, vol. 14, no. 2, pp. 585–592, Jun. 2013, doi: 10.1208/S12249-013-9943-3/FIGURES/6.

[110] B. Lu, X. Lv, and Y. Le, "Chitosan-Modified PLGA Nanoparticles for Control-Released Drug Delivery," *Polym. 2019, Vol. 11, Page 304*, vol. 11, no. 2, p. 304, Feb. 2019, doi: 10.3390/POLYM11020304.

[111] S. Khanal, U. Adhikari, N. P. Rijal, S. R. Bhattarai, J. Sankar, and N. Bhattarai, "pH-Responsive PLGA Nanoparticle for Controlled Payload Delivery of Diclofenac Sodium," *J. Funct. Biomater. 2016, Vol. 7, Page 21*, vol. 7, no. 3, p. 21, Aug. 2016, doi: 10.3390/JFB7030021.

[112] V. Khare *et al.*, "Synthesis, characterization and mechanistic-insight into the anti-proliferative potential of PLGA-gemcitabine conjugate," *Int. J. Pharm.*, vol. 470, no. 1–2, pp. 51–62, Aug. 2014, doi: 10.1016/J.IJPHARM.2014.05.005.

[113] L. R. Jaidev, U. M. Krishnan, and S. Sethuraman, "Gemcitabine loaded biodegradable PLGA nanospheres for in vitro pancreatic cancer therapy," *Mater. Sci. Eng. C*, vol. 47, pp. 40–47, Feb. 2015, doi: 10.1016/J.MSEC.2014.11.027.

[114] A. Zeb, M. Gul, T. T. L. Nguyen, and H. J. Maeng, "Controlled release and targeted drug delivery with poly(lactic-co-glycolic acid) nanoparticles: reviewing two decades of research," *J. Pharm. Investig. 2022 526*, vol. 52, no. 6, pp. 683–724, Jul. 2022, doi: 10.1007/S40005-022-00584-W.

[115] P. Bihari *et al.*, "Optimized dispersion of nanoparticles for biological in vitro and in vivo studies," *Part. Fibre Toxicol.*, vol. 5, p. 14, Nov. 2008, doi: 10.1186/1743-8977-5-14.

[116] T. A. Zughaibi *et al.*, "Evaluation of Anticancer Potential of Biogenic Copper Oxide Nanoparticles (CuO NPs) against Breast Cancer," *J. Nanomater.*, vol. 2022, 2022, doi: 10.1155/2022/5326355.

[117] E. Lagreca, V. Onesto, C. Di Natale, S. La Manna, P. A. Netti, and R. Vecchione, "Recent advances in the formulation of PLGA microparticles for controlled drug delivery," *Prog. Biomater. 2020 94*, vol. 9, no. 4, pp. 153–174, Oct. 2020, doi: 10.1007/S40204-020-00139-Y.

[118] "PubChem Compound Summary for CID 60750, Gemcitabine," National Center for Biotechnology Information, PubChem 2004. [Online] Available: https://pubchem.ncbi.nlm.nih.gov/compound/Gemcitabine#section=ChEMBL-ID.

56 References

Appendix

A1. Calibration Curves

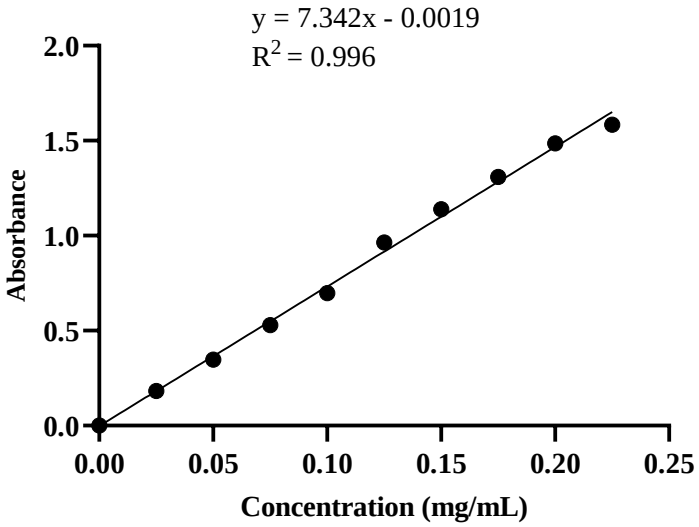

Figure A1.1 – Absorbance calibration curve of GEM in PVA 1%.

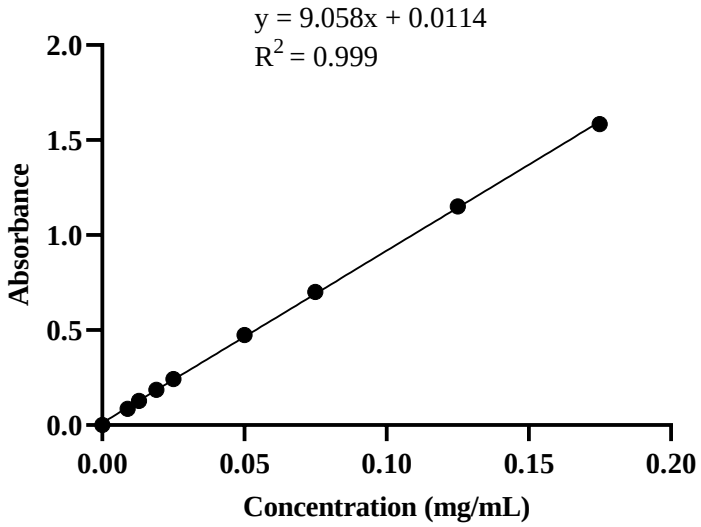

Figure A1.2 – Absorbance calibration curve of GEM in PBS (pH 7.4).

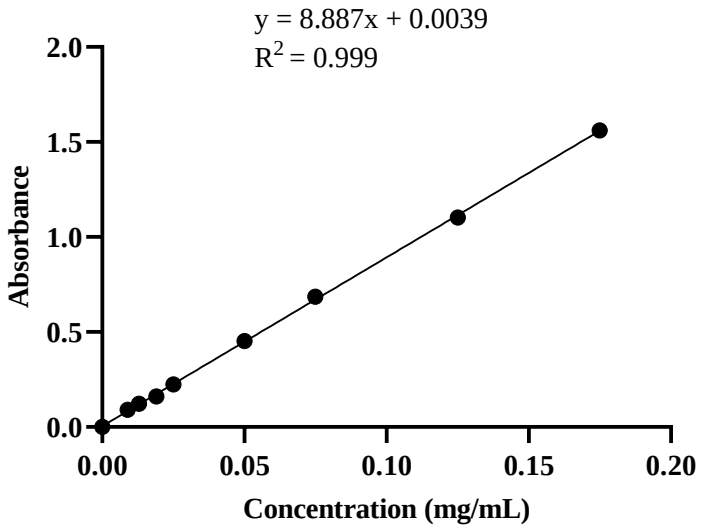

Figure A1.3 – Absorbance calibration curve of GEM in PBS (pH 6.4).

A2. Experimental Design

Table A2.1 - ANOVA analysis for the response variable Size applying a quartic model.

Response: Size						
Source	**Sum of Squares**	**df**	**Mean Square**	**F-value**	**p-value**	
Model	5.299E+05	24	22079.11	680.61	0.0015	significant
A-PLGA	307.52	1	307.52	9.48	0.0913	
B-PVA	32410.58	1	32410.58	999.09	0.0010	
C-EA	2.413E+05	1	2.413E+05	7438.47	0.0001	
D-Sonication cycles	812.05	1	812.05	25.03	0.0377	
AB	862.89	1	862.89	26.60	0.0356	
AC	363.86	1	363.86	11.22	0.0788	
AD	0.2756	1	0.2756	0.0085	0.9350	
BC	2335.31	1	2335.31	71.99	0.0136	
BD	13.51	1	13.51	0.4163	0.5849	
CD	2.33	1	2.33	0.0717	0.8140	
A^2	2376.30	1	2376.30	73.25	0.0134	
B^2	20186.51	1	20186.51	622.27	0.0016	
C^2	1.642E+05	1	1.642E+05	5062.75	0.0002	
D^2	3544.71	1	3544.71	109.27	0.0090	
ABC	2013.77	1	2013.77	62.08	0.0157	
ABD	611.33	1	611.33	18.84	0.0492	
ACD	1.05	1	1.05	0.0324	0.8738	
BCD	5.88	1	5.88	0.1813	0.7117	
A^2B	18657.36	1	18657.36	575.13	0.0017	
A^2C	1.860E+05	1	1.860E+05	5732.20	0.0002	
A^2D	98.03	1	98.03	3.02	0.2243	
AB^2	357.48	1	357.48	11.02	0.0800	
ABCD	209.53	1	209.53	6.46	0.1262	
A^2B^2	95704.35	1	95704.35	2950.20	0.0003	
Pure Error	64.88	2	32.44			
Cor Total	5.300E+05	26				

Table A2.2 - ANOVA analysis for the response variable PDI applying a quadratic model.

Response: PDI						
Source	**Sum of Squares**	**df**	**Mean Square**	**F-value**	**p-value**	
Model	0.0992	14	0.0071	1.28	0.3400	not significant
A-PLGA	0.0082	1	0.0082	1.47	0.2479	
B-PVA	0.0131	1	0.0131	2.35	0.1509	
C-EA	0.0010	1	0.0010	0.1717	0.6859	
D-Sonication cycles	0.0021	1	0.0021	0.3861	0.5460	
AB	0.0002	1	0.0002	0.0328	0.8593	
AC	0.0089	1	0.0089	1.61	0.2288	
AD	1.000E-06	1	1.000E-06	0.0002	0.9895	
BC	0.0044	1	0.0044	0.7963	0.3897	
BD	0.0040	1	0.0040	0.7147	0.4144	
CD	0.0032	1	0.0032	0.5850	0.4591	
A^2	0.0282	1	0.0282	5.07	0.0438	
B^2	0.0248	1	0.0248	4.46	0.0563	
C^2	0.0010	1	0.0010	0.1856	0.6742	
D^2	0.0001	1	0.0001	0.0097	0.9230	
Residual	0.0666	12	0.0056			
Lack of Fit	0.0639	10	0.0064	4.66	0.1896	not significant
Pure Error	0.0027	2	0.0014			
Cor Total	0.1658	26				

Table A2.3 - ANOVA analysis for the response variable Zeta Potential applying a quartic model.

Response: Zeta Potential						
Source	**Sum of Squares**	**df**	**Mean Square**	**F-value**	**p-value**	
Model	1875.67	24	78.15	366.34	0.0027	significant
A-PLGA	2.88	1	2.88	13.50	0.0667	
B-PVA	70.80	1	70.80	331.90	0.0030	
C-EA	438.08	1	438.08	2053.50	0.0005	
D-Sonication cycles	14.04	1	14.04	65.84	0.0149	
AB	1.05	1	1.05	4.92	0.1567	
AC	20.48	1	20.48	95.98	0.0103	
AD	7.16	1	7.16	33.54	0.0285	
BC	62.81	1	62.81	294.40	0.0034	
BD	20.48	1	20.48	95.98	0.0103	
CD	5.64	1	5.64	26.44	0.0358	
A^2	47.13	1	47.13	220.90	0.0045	
B^2	0.2083	1	0.2083	0.9766	0.4272	
C^2	300.83	1	300.83	1410.16	0.0007	
D^2	8.86	1	8.86	41.51	0.0233	
ABC	12.43	1	12.43	58.25	0.0167	
ABD	1.63	1	1.63	7.62	0.1100	
ACD	86.96	1	86.96	407.60	0.0024	
BCD	46.58	1	46.58	218.35	0.0045	
A^2B	0.0547	1	0.0547	0.2564	0.6629	
A^2C	212.74	1	212.74	997.21	0.0010	
A^2D	72.76	1	72.76	341.06	0.0029	
AB^2	2.17	1	2.17	10.18	0.0858	
ABCD	0.0156	1	0.0156	0.0732	0.8120	
A^2B^2	25.33	1	25.33	118.73	0.0083	
Pure Error	0.4267	2	0.2133			
Cor Total	1876.10	26				

Table A2.4 - ANOVA analysis for the response variable EE applying a quadratic model.

Response: EE						
Source	**Sum of Squares**	**df**	**Mean Square**	**F-value**	**p-value**	
Model	1795.05	14	128.22	6.66	0.0011	significant
A-PLGA	4.00	1	4.00	0.2076	0.6568	
B-PVA	354.74	1	354.74	18.41	0.0010	
C-EA	213.78	1	213.78	11.10	0.0060	
D-Sonication cycles	167.35	1	167.35	8.69	0.0122	
AB	68.89	1	68.89	3.58	0.0830	
AC	57.00	1	57.00	2.96	0.1111	
AD	16.81	1	16.81	0.8726	0.3687	
BC	605.16	1	605.16	31.41	0.0001	
BD	11.90	1	11.90	0.6178	0.4471	
CD	14.44	1	14.44	0.7496	0.4036	
A^2	0.9903	1	0.9903	0.0514	0.8244	
B^2	91.22	1	91.22	4.74	0.0502	
C^2	186.10	1	186.10	9.66	0.0091	
D^2	2.66	1	2.66	0.1382	0.7166	
Residual	231.18	12	19.26			
Lack of Fit	213.57	10	21.36	2.43	0.3271	not significant
Pure Error	17.61	2	8.80			
Cor Total	2026.23	26				

A2.5 – Equation: Size

$$\textbf{Size} = 161.50 + 8.02A - 82.30B - 224.57C - 13.03D - 7.34AB + 12.08BC + 18.60A^2 + 54.22B^2 + 154.64C^2 + 22.72D^2 + 11.22ABC + 6.18ABD + 71.17A^2B + 224.69A^2C + 5.16A^2D + 9.85AB^2 + 3.62ABCD - 232.02A^2B^2 \quad \text{(A2.5)}$$

Legend: PLGA mass (A), %PVA (B), Volume of EA (C) and number of sonication cycles (D).

A2.6 – Equation: Zeta Potencial

$$\textbf{Zeta Potential} = 20.77 - 0.7758A - 3.85B - 9.57C + 1.71D + 1.13AC + 0.6687AD + 1.98BC - 1.13BD + 0.5937CD - 2.62A^2 + 6.62C^2 - 1.14D^2 + 0.8813ABC - 2.33ACD - 1.71BCD + 7.60A^2C - 4.44A^2D - 3.77A^2B^2 \quad \text{(A2.6)}$$

Legend: PLGA mass (A), %PVA (B), Volume of EA (C) and number of sonication cycles (D).

A2.7 – Equation: EE

$$\textbf{EE} = 27.66 - 0.4387A + 4.13B - 3.21C + 2.84D + 6.15BC + 4.03C^2 \quad \text{(A2.7)}$$

Legend: PLGA mass (A), %PVA (B), Volume of EA (C) and number of sonication cycles (D).

A3. Gemcitabine solubility studies

PLGA NPs can be prepared by a single-emulsion or double emulsion-evaporation method depending on the hydrophobicity of the drug [117]. The solubility of GEM was tested in the most used solvents for NPs preparation, to choose the most suitable for the experiments. Since the high solubility of GEM in water is well-reported in the literature (up to 51.3 mg/mL) [118], for this solvent it was only confirmed that it was possible to dissolve GEM at the concentration required for NPs preparation (2 mg/mL). The solubility test was applied to the following solvents: ethyl acetate, dimethyl sulfoxide (DMSO), and dichloromethane. The procedure for testing the solubility of GEM started with the preparation of solutions of GEM in the solvents at a concentration of 2.0 mg/mL. All prepared solutions were subjected to a sequence of procedures, starting with 5 to 10 min of mechanical stirring using a vortex (Heidolph Reax Top Vortex Mixer, Heidolph instruments GmbH & Co., Schwabach, Germany), followed by 10 min of sonication at an ultrasonic frequency of 45 kHz (ultrasonic bath, Ultrasonic cleaner, VWRTM, Malasya) with no temperature applied and then 10 min of sonication at 37 ºC. If after this set of procedures, GEM was still not completed dissolved in the solvent under study, a solution with a concentration of 1.0 mg/mL of GEM in the solvent was prepared and the 3 steps already listed were repeated. GEM solubility was then confirmed by naked eye and UV-Vis absorbance measurements between 200 and 700 nm (Synergy 2 Microplate Reader, BioTek, UK).

After choosing the most adequate solvent, the stability of the drug in the NPs preparation experimental conditions was evaluated. For that, a 2.0 mg/mL solution was subjected to the NPs preparation conditions. These conditions consisted of 6 cycles of 10 seconds of on-off sonication at a 70% of amplification and an ultrasonic frequency of 24 kHz (UP400S ultrasonic processor, Hielscher, Berlin, Germany) plus mechanical vortex stirring. To evaluate the solvent stability, the UV-Vis absorbance of the solution was measured before and after the described procedure.

The solubility studies demonstrated that GEM is not soluble in ethyl acetate and dichloromethane since all steps mentioned were performed for both, and no solubilization of GEM occurred. More specifically, for a concentration of 1.0 mg/mL of GEM in each of the solvents, there was no solubility when the solutions were subjected to 10 min of sonication at 37 ºC. Regarding DMSO, it was possible to solubilize GEM at a concentration of 2.0 mg/mL after 10 min of mechanical stirring. To test whether solubilization was at its maximum, the UV-Vis absorbance of the solution was evaluated. Two measurements were performed, an initial measurement (after the first 10 min in the vortex) and a final measurement, of the same solution, but with a repeat of the 10 min of mechanical stirring (making a total of 20 min). As shown in figure 7, the initial absorbance measurement at λ_{max} 271 nm was 1.239 and the final absorbance measurement was 1.485.

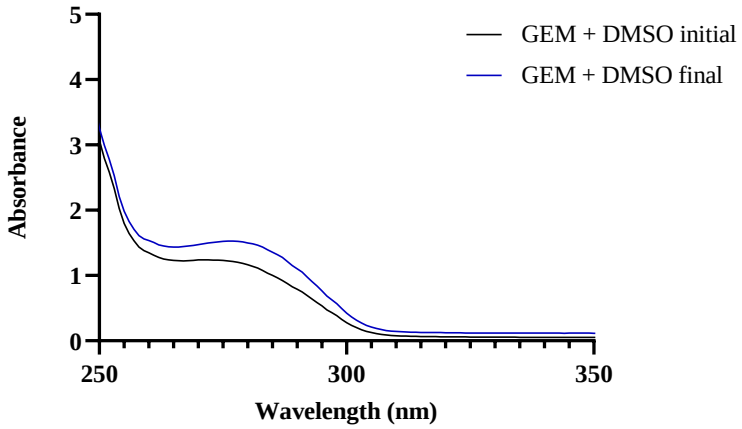

Figure A3.1 - Solubility of GEM in DMSO, where GEM+DMSO initial and final refers to the measurement made with 10 min and 20 min of mechanical stirring, respectively.

The absorbance increased slightly, so it can be stated that in the first measurement, GEM was not totally dissolved. Absorbance is proportional to concentration, which means that this increase in absorbance value was due to an increase in the concentration of GEM in DMSO, as there was further solubilization of the solute in the solvent.

The solvent chosen for the dilution of GEM was ultrapure water, given its ease of solubilization. To assess the drug stability, the absorbance of GEM in ultrapure water was measured before and after the sample being subjected to the NPs preparation conditions, as represented in the figure 8 below.

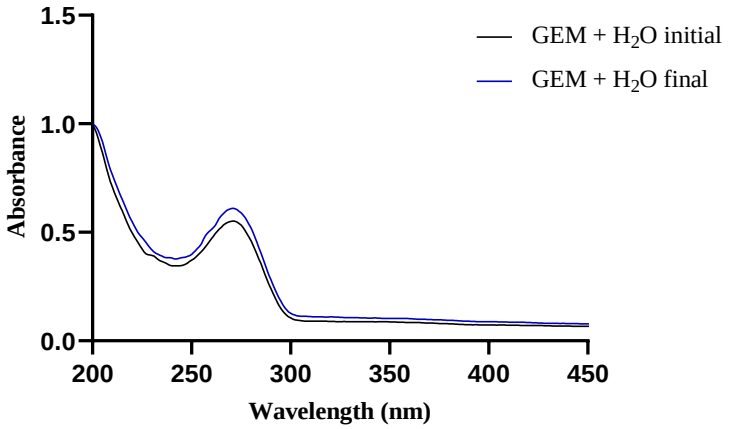

Figure A3.2 - Stability of GEM in ultrapure water, where GEM+H_2O initial and final refers to the measurement made before the solution was subjected to the NPs preparation conditions and after, respectively.

A slight increase was verified in the final spectrum which may occur due to water evaporation when subjected to the circumstances of preparation of the NPs, since these consisted of sonication and mechanical agitation. Thus, it was concluded that the GEM remained stable when subjected to the experimental conditions, and therefore water could be used as suitable solvent for NPs preparation.